

1N-02
54319

NASA Technical Memorandum 4660

p. 35



Drag Measurements of an Axisymmetric Nacelle Mounted on a Flat Plate at Supersonic Speeds

Jeffrey D. Flamm and Floyd J. Wilcox, Jr.

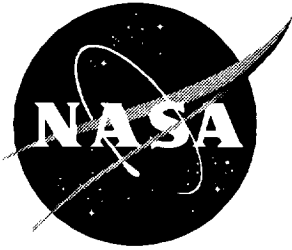
(NASA-TM-4660) DRAG MEASUREMENTS
OF AN AXISYMMETRIC NACELLE MOUNTED
ON A FLAT PLATE AT SUPERSONIC
SPEEDS (NASA Langley Research
Center) 35 p

N95-32821

Unclass

H1/02 0055819

June 1995



Drag Measurements of an Axisymmetric Nacelle Mounted on a Flat Plate at Supersonic Speeds

*Jeffrey D. Flamm and Floyd J. Wilcox, Jr.
Langley Research Center • Hampton, Virginia*

Available electronically at the following URL address: <http://techreports.larc.nasa.gov/ltrs/ltrs.html>

Printed copies available from the following:

NASA Center for Aerospace Information
800 Elkridge Landing Road
Linthicum Heights, MD 21090-2934
(301) 621-0390

National Technical Information Service (NTIS)
5285 Port Royal Road
Springfield, VA 22161-2171
(703) 487-4650

Abstract

An experimental investigation was conducted to determine the effect of diverter wedge half-angle and nacelle lip height on the drag characteristics of an assembly consisting of a nacelle fore cowl from a typical high-speed civil transport (HSCT) and a diverter mounted on a flat plate. Data were obtained for diverter wedge half-angles of 4.0°, 6.0°, and 8.0° and ratios of the nacelle lip height above a flat plate to the boundary-layer thickness (h_n/δ) of approximately 0.87 to 2.45. Limited drag data were also obtained on a complete nacelle/diverter configuration that included fore and aft cowls. Although the nacelle/diverter drag data were not corrected for base pressures or internal flow drag, the data are useful for comparing the relative drag of the configurations tested. The tests were conducted in the Langley Unitary Plan Wind Tunnel at Mach numbers of 1.50, 1.80, 2.10, and 2.40 and Reynolds numbers ranging from 2.00×10^6 to 5.00×10^6 per foot. The results of this investigation showed that the nacelle/diverter drag essentially increased linearly with increasing h_n/δ except near 1.0 where the data showed a nonlinear behavior. This nonlinear behavior was probably caused by the interaction of the shock waves from the nacelle/diverter configuration with the flat-plate boundary layer. At the lowest h_n/δ tested, the diverter wedge half-angle had virtually no effect on the nacelle/diverter drag. However, as h_n/δ increased, the nacelle/diverter drag increased as diverter wedge half-angle increased.

Introduction

The renewed interest in high-speed civil transport (HSCT) configurations with extended supersonic range has spurred investigations into aircraft drag reduction at supersonic cruise conditions. Mutual aerodynamic interference between the engine nacelles and airframe can have a significant impact on efficient propulsion-airframe integration. By paying close attention to the flow field interactions of the nacelle and airframe, the designer can exploit the favorable interference effects to minimize the total aircraft drag (refs. 1–4).

Linear analysis methods have been shown to roughly predict the drag levels and basic interference effects associated with nacelle-airframe interaction (refs. 4–7). Also, linear design methods (refs. 3 and 8) have been fairly effective in improving the overall integrated drag characteristics. However, a more detailed and accurate understanding of nacelle-airframe integration characteristics is needed to support the development and application of advanced computational fluid dynamics (CFD) analysis and design methods.

Numerous experimental studies have been conducted to identify the basic interaction of the nacelle and airframe and to evaluate various analysis and design methodologies. Typically, the nacelle drag increment is obtained by subtracting the clean aircraft drag from the drag of the aircraft with nacelles (refs. 2 and 9–11). The primary advantage of this technique is that it is a generally accepted method to obtain the installed nacelle drag.

The primary disadvantage of this technique is that separating the various drag components that contribute to the total installed nacelle drag is impossible. These include nacelle-on-aircraft interference drag, aircraft-on-nacelle interference drag, nacelle-on-nacelle interference drag, and isolated nacelle drag. Another disadvantage of this technique is that the data accuracy suffers because the strain-gauge balance must be selected to measure the drag of the entire model instead of just the nacelles.

Another technique that has been used to measure nacelle drag increments was developed at the Ames Research Center (ref. 5). In this technique, the aircraft model is mounted to one strain-gauge balance and support mechanism, whereas the nacelles are mounted on an independent flow-through strain-gauge balance and model support mechanism. This technique allows the nacelles to be positioned anywhere underneath the aircraft wing. The primary advantage of this technique is that the various drag components previously discussed can be determined from the separate aircraft and nacelle drag measurements. In addition, the accuracy of the nacelle drag measurements is improved because the nacelle strain-gauge balances are sized to measure only the nacelle drag. However, this technique is limited in that the nacelle diverters are not modeled.

Recent experimental store-carriage drag studies at the Langley Research Center have been useful in determining the drag characteristics of isolated stores as well as the mutual interference between stores that were mounted on a flat plate (ref. 12). In this technique, the

drag of an isolated store mounted on a flat plate was measured with a strain-gauge balance such that only the drag of the store was measured and not the drag of the entire flat plate. Accurate drag measurements were obtained by using this method because the strain-gauge balance was sized to measure the drag of a single store. The hardware used for the store-carriage drag studies was readily available and easily adaptable to conduct tests to measure the drag of a nacelle/diverter configuration. The flat plate eliminated any interference effects from the complicated flow field of an aircraft and provided a uniform two-dimensional flow field for testing a nacelle and diverter. In addition, the geometric simplicity of the flat plate was an ideal case for initial CFD code-validation studies.

The purpose of this study was to determine the effect of diverter wedge half-angle and nacelle lip height on the drag characteristics of an assembly of a typical HSCT nacelle fore cowl and a diverter. The nacelle lip height was varied by changing the diverter height. Also, limited data were obtained on a complete nacelle/diverter configuration that included an aft cowl. Boundary-layer profiles on the flat-plate surface were obtained to determine the boundary-layer thickness approaching the nacelle/diverter configuration. Although the nacelle/diverter drag data were not corrected for base pressures or internal flow drag, the data are useful for comparing the relative drag between configurations tested. These tests were conducted at Mach numbers of 1.50, 1.80, 2.10, and 2.40 and at Reynolds numbers ranging from 2.00×10^6 to 5.00×10^6 per foot.

Symbols and Abbreviations

A_l	area of pallet lip, 0.0009201 ft ²
C_D	drag coefficient, $\frac{\text{Drag force}}{q_\infty S}$
C_p	pressure coefficient, $\frac{p - p_\infty}{q_\infty}$
D	drag force, lb
h	height of boundary-layer probe tube above flat plate, in. (see fig. 1(b))
h_d	height of diverter, in. (see fig. 3(b))
h_n	height of nacelle lip above flat plate, in. (see fig. 3(b))
h_r	height of nacelle centerline above flat plate, in. (see fig. 3(b))
M	free-stream Mach number
p	measured pressure, lb/ft ²
p_∞	free-stream static pressure, lb/ft ²
p_0	free-stream stagnation pressure, lb/ft ²

$p_{0,2}$	free-stream stagnation pressure immediately behind shock wave, lb/ft ²
q_∞	dynamic pressure, lb/ft ²
R	free-stream Reynolds number, per foot
S	reference area, 2.602 ft ²
T_0	free-stream stagnation temperature, °F
δ	measured boundary-layer thickness, in.
θ	diverter wedge half-angle, deg

Apparatus and Experimental Methods

Model Description

A photograph and schematic diagram of the flat plate are shown in figure 1. The flat plate was 30.00 in. long with a maximum span of 34.00 in. The leading edge of the plate directly in front of the nacelle/diverter model had a sweep angle of 0° in order to provide a uniform two-dimensional boundary layer approaching the nacelle/diverter model. The outboard leading edges were swept 30°. This sweep served three purposes: (1) to decrease the plate planform area to reduce starting loads; (2) to position the disturbance from tip vortices downstream in order to minimize their effect on the flat-plate flow field; and (3) to ensure that Mach lines produced by the tips would propagate downstream of the metric nacelle/diverter location. The leading-edge wedge half-angle (5°) on the lower surface was sufficiently small to maintain supersonic attached flow at the leading edge throughout the Mach number range.

A cavity that housed the strain-gauge balance and pressure tubing was located on the upper surface centerline of the plate and was covered by a filler plate, as shown in figures 1(b) and 2. The instrumentation cavity was vented to the plate surface with four multihole vents (fig. 1(b)) to reduce the normal force on the pallet and strain-gauge balance during tunnel start-up and shutdown. A pallet, which was located within a cutout in the filler plate, was mounted on a one-component strain-gauge balance such that the top surface of the pallet was flush with the flat-plate surface. Although not shown, the pallet actually consisted of two separate parts (pallet insert and pallet base) to facilitate model changes. The pallet was isolated from the filler plate by two air gaps, as shown in figure 1(b). The 0.005-in. horizontal gap allowed the pallet-balance combination to deflect. The 0.003-in. vertical gap minimized the airflow to and from the flat-plate surface and the instrumentation cavity. Boundary-layer surveys conducted on the pallet with and without a foam seal covering the 0.003-in. gap showed similar results, thereby indicating that flow was negligible through the gap. Details of these surveys are contained in appendix A.

In addition, four static pressure orifices were located in the instrumentation cavity to verify that the flow was negligible through the gap between the pallet assembly and filler plate. As shown in figure 2, three static pressure orifices were located on the fore and aft lips of the pallet insert and at mirrored locations on the filler plate to correct the drag data for pressure forces on the pallet. However, initial checkruns showed only a minimal difference between the pressures on the pallet and filler plate. To eliminate the tare load on the strain-gauge balance caused by the pallet pressure tubing, the tubes on the pallet were disconnected for the entire test. Only the pressure tubes on the filler plate were used to correct the pallet lip pressure drag.

Figure 3 shows a photograph and sketch of a typical nacelle/diverter assembly, and photographs and a detailed sketch of the nacelle and diverters are shown in figures 4 and 5, respectively. The axisymmetric nacelle had a constant-area circular flow-through duct and a removable aft cowl. The nine diverters tested had leading-edge wedge half-angles (θ) of 4.0°, 6.0°, and 8.0° and heights (h_d) of 0.19, 0.34, and 0.44 in. at the leading edge. The diverters were constructed such that the centerline of the nacelle remained parallel to the flat-plate surface as the diverter height was increased. At the lowest diverter height, the aft end of the nacelle fore cowl was on the flat-plate surface, as shown in figure 5(b).

A boundary-layer survey was conducted on the flat-plate upper surface centerline at the streamwise location where the plane of the nacelle inlet intersected the flat plate. This survey was used to determine the boundary-layer thickness (δ) at the nacelle inlet face. The details of the boundary-layer survey are presented in appendix A. Because making a model change to vary the nacelle lip height at each test condition was impractical to account for the varying boundary-layer thicknesses, the nacelle lip was positioned at fixed heights (h_n) ranging from

0.20 to 0.49 in., which corresponds to 0.878 to 2.458 at $M = 2.40$ and $R = 2.00 \times 10^6$ per foot. Shims were placed under the diverter to provide fine adjustments to the nacelle lip heights. The nacelle lip heights were non-dimensionalized by the actual measured boundary-layer thickness at each test condition.

Wind Tunnel and Test Conditions

The investigation was conducted in test section 1 of the Langley Unitary Plan Wind Tunnel (UPWT), which is a variable-pressure continuous-flow facility. An asymmetric sliding-block nozzle allows the Mach number to be varied continuously from approximately 1.46 to 2.86 in the low Mach number test section (test section 1). This test section measures approximately 4-by 4-ft in cross section and 7 ft in length. A complete description of the tunnel and its calibration can be found in reference 13.

A listing of the test conditions can be found in table I. The angle of attack of the flat plate was held constant at 0° throughout the entire test. The dew point of the tunnel air was maintained at appropriate levels to prevent water-vapor condensation effects at all test conditions. Grit-type boundary-layer transition strips were applied to the flat plate, nacelle, and diverter leading edges to ensure a fully turbulent boundary layer. Transition strips were applied to both the internal and external surfaces of the nacelle. The transition strips consisted of No. 60 sand grit (0.0107-in. nominal height) sprinkled in a lacquer film along a strip 0.1 in. wide and located 0.4 in. aft of the leading edge measured streamwise on the flat plate, nacelle, and diverters. The grit size and location were selected according to the standard procedures for testing in the Langley UPWT (ref. 14). These procedures are based on unpublished transition experiments conducted in the UPWT and on the methods of references 15 and 16.

Measurements and Corrections

The nacelle/diverter drag was measured with a one-component (axial force) electrical strain-gauge balance. This measured drag was composed of several parts as shown below:

$$(D)_{\text{measured}} = (D)_{\text{nacelle/diverter}} + (D)_{\text{pallet skin friction}} + (D)_{\text{pallet lip pressures}} \quad (1)$$

The drag of the nacelle/diverter configuration can be further broken down as follows:

$$(D)_{\text{nacelle/diverter}} = (D)_{\text{nacelle/diverter external pressure and skin friction, excluding base pressure}} + (D)_{\text{nacelle internal pressure and skin friction}} + (D)_{\text{nacelle/diverter base pressure}} \quad (2)$$

Thus, the measured drag can be expressed as

$$(D)_{\text{measured}} = (D)_{\text{nacelle/diverter external pressure and skin friction, excluding base pressure}} + (D)_{\text{nacelle internal pressure and skin friction}} + (D)_{\text{nacelle/diverter base pressure}} + (D)_{\text{pallet skin friction}} + (D)_{\text{pallet lip pressures}} \quad (3)$$

For this particular test, the measured drag was corrected only for the pallet lip pressures. Therefore, all drag data presented in this report contain the components of drag from the first four terms on the right-hand side of equation (3). Thus,

$$(D)_{\text{corrected}} = (D)_{\text{measured}} - (D)_{\text{pallet lip pressures}} = (D)_{\text{nacelle/diverter external pressure and skin friction, excluding base pressure}} + (D)_{\text{nacelle internal pressure and skin friction}} + (D)_{\text{nacelle/diverter base pressure}} + (D)_{\text{pallet skin friction}} \quad (4)$$

The second term on the right-hand side of equation (4), commonly referred to as "internal flow drag," was not corrected because this investigation was primarily concerned with the relative effects of diverter wedge half-angle and nacelle lip height rather than the absolute nacelle/diverter drag. Since the nacelle was outside the flat-plate boundary layer for all cases except the lowest nacelle lip height, the nacelle internal flow drag should have been constant or nearly constant for all configurations except those in which the nacelle lip was slightly submerged in the boundary layer. Therefore, the relative effects of the nacelle lip height and diverter wedge half-angle can be discerned from the data; however, caution should be exercised when conclusions are drawn from the data where the nacelle lip is slightly submerged in the boundary layer.

The third term in equation (4) is the nacelle/diverter base pressure drag. Base pressure measurements were attempted during this test by placing a four-probed rake downstream of the nacelle/diverter configuration. Drag measurements obtained with and without the rake installed indicated that the rake was affecting the drag of the nacelle/diverter combination. The force data did not show whether the rake was only changing the base pressures or if it was affecting the entire nacelle/diverter flow field. Therefore, the base pressure rake was not used during this test, and consequently, the nacelle/diverter base pressures were not measured during this test. Although the drag data presented in this paper are not corrected for base pressure drag, the analysis of the drag data presented in the "Results and Discussion" section notes possible base pressure effects.

Finally, the last term on the right-hand side of equation (4) is the skin-friction drag on the exposed portion of the pallet forward and aft of the diverter. (See fig. 3(a).) The pallet skin friction was estimated by assuming that a

flat-plate flow field existed over the pallet. These calculations used measured skin-friction drag data from a different pallet on this same flat plate scaled to the current pallet size (ref. 17). These estimates represent an upper limit assessment because in the actual nacelle tests, the aft part of the pallet was in the wake of the nacelle and diverter and therefore should have a lower skin friction than if the nacelle and diverter were not on the pallet. The calculations showed that the pallet skin-friction drag was on the order of 1 percent of the measured nacelle/diverter drag. Because of the difficulty in accurately estimating the pallet skin-friction drag and because the relative effects of the nacelle lip height and diverter wedge half-angle can be discerned from the measured data, the drag data were not corrected for the pallet skin-friction drag.

As was mentioned previously, all drag data have been corrected for the pressure drag on the forward and aft lips of the pallet. The correction for pallet lip pressure was calculated by averaging the three measured pressures on the forward lips and the three pressures on the aft lips and then applying the average to the appropriate lip areas. The pallet lip pressures were measured by using an electronically scanned 5-psi pressure transducer, and the tunnel stagnation pressure was measured by using a 100-psi pressure transducer.

A reference area (S), representative of a typical wind-tunnel-model-scale HSCT configuration, was used to nondimensionalize the drag data in this study to provide nacelle/diverter drag coefficient data that are comparable to a complete HSCT configuration. The reference area used in this study was determined by first calculating the ratio of the wing reference area to the total nacelle frontal area of three typical supersonic transport (SST) configurations that were tested in the early 1970's. (See refs. 9-11.) These three ratios were then

averaged. By assuming that a typical HSCT configuration has four nacelles, the averaged ratio (calculated above) of wing reference area to nacelle frontal area was multiplied by the frontal area of four present nacelles to obtain the reference area of 2.602 ft², the area used in this report.

The uncertainty of the drag measurements was calculated with the method discussed in appendix B. The largest uncertainty in C_D at each Mach number is given as follows:

M	Uncertainty in C_D
1.50	± 0.000013
1.80	$\pm .000017$
2.10	$\pm .000020$
2.40	$\pm .000021$

The repeatability of the drag data was generally much better than the uncertainty, although the repeatability was dependent on Mach number. Repeatability in this case is defined as the ability to obtain the same drag value from taking several data points (approximately four or five) in short succession (approximately 20 sec apart) and the ability to obtain the same drag value on a configuration that has been tested two or more times (during the same tunnel entry) with other configurations in between. For this test, the repeatability of the drag coefficient data for Mach numbers from 1.50 to 2.10 was approximately ± 0.03 counts (± 0.000003), whereas the repeatability at a Mach number of 2.40 was approximately ± 0.1 counts. A listing of the drag data obtained during this test is contained in table II.

Results and Discussion

The results from this investigation are divided into four major areas: effect of nacelle lip height, effect of diverter wedge half-angle, effect of aft cowl, and effect of Reynolds number.

Effect of Nacelle Lip Height

Figure 6 shows the effect of nacelle lip height on nacelle/diverter drag for the three different diverter wedge half-angles ($\theta = 4.0^\circ$, 6.0° , and 8.0°) for the nacelle without an aft cowl. At all test Mach numbers, the drag increases nearly linearly with increasing h_n/δ . At any given h_n/δ , the nacelle/diverter drag generally increases with increasing θ , as would be expected. At

the lowest h_n/δ , the data tend to collapse into a narrow band, which indicates that within the boundary layer the diverter wedge half-angle has very little effect on drag.

Effect of Diverter Wedge Half-Angle

Figure 7 is a cross plot of the data presented in figure 6 to further emphasize the effect of diverter wedge half-angle on the drag of the nacelle/diverter configuration without an aft cowl. As mentioned previously, the diverter wedge half-angle had very little effect at the lowest h_n/δ , but the effect became more pronounced as the nacelle was moved farther from the flat plate and a larger portion of the diverter was outside the boundary layer. In general, the largest drag increase occurred as the diverter wedge half-angle (θ) was increased from 6.0° to 8.0° .

Effect of Aft Cowl

The effect of h_n/δ on drag coefficient for the nacelle/diverter assembly with and without an aft cowl attached is shown in figure 8. The data generally increase linearly with increasing h_n/δ , although some nonlinearity is evident at the lowest h_n/δ point obtained at all Mach numbers. These nonlinearities are believed to be caused by interactions between the shock waves from the nacelle/diverter assembly with the flat-plate boundary layer as the nacelle is moved closer to the flat-plate surface. The primary effect of adding the aft cowl to the nacelle/diverter assembly is a decrease in the magnitude of the nacelle/diverter drag. At $M = 1.50$ and $M = 1.80$, the reduction in drag is generally constant (figs. 8(a) and 8(b)). At $M = 2.10$ and $M = 2.40$, the distance between the two curves decreases as h_n/δ increases (figs. 8(c) and 8(d)). This drag reduction is probably caused by two primary factors: the reduced base area of the aft cowl as compared with the fore cowl and the favorable pressure gradient caused by the boattail effect of the aft cowl. Because no base pressure measurements were obtained, determining the magnitude of these two effects on the nacelle/diverter drag reduction is not possible.

Effect of Reynolds Number

Figure 9 shows the effect of Reynolds number on nacelle/diverter drag for a diverter wedge half-angle of 8.0° and a fixed nacelle lip height of 0.24 in. The maximum strain-gauge balance load restricted the data obtained at lower Mach numbers. Generally, C_D decreased with increasing Reynolds number; this decrease was due primarily to the skin-friction drag reduction as Reynolds number increased. The exception

to this trend may be due to the uncertainty of the data at a Mach number of 2.40.

Conclusions

An experimental investigation was conducted to determine the effect of diverter wedge half-angle and nacelle lip height on the drag characteristics of an assembly consisting of a nacelle fore cowl from a typical high-speed civil transport (HSCT) and a diverter mounted on a flat plate. Data were obtained for diverter wedge half-angles of 4.0°, 6.0°, and 8.0° and ratios of the nacelle lip height above a flat plate to the boundary-layer thickness (h_n/δ) of approximately 0.87 to 2.45. Limited drag data were also obtained on a complete nacelle/diverter configuration that included fore and aft cowls. Although the nacelle/diverter drag data were not corrected for base pressures or internal flow drag, the data are useful for comparing the relative drag of the configurations tested. The tests were conducted at Mach numbers of 1.50, 1.80, 2.10, and 2.40 and Reynolds numbers ranging from 2.00×10^6 to 5.00×10^6 per foot. The following conclusions are presented from this study:

1. The drag of the nacelle/diverter configuration generally increased linearly with increasing h_n/δ .
2. The drag of the nacelle/diverter configuration generally increased as the diverter wedge half-angle (θ) increased; however, this effect was less pronounced as h_n/δ decreased. At the lowest h_n/δ tested, the nacelle/diverter drag was generally not affected by θ .
3. The primary effect of adding the aft cowl to the combination of a nacelle fore cowl and diverter was a decrease in the magnitude of the nacelle/diverter drag. This reduction can be partially attributed to the reduced base area of the aft cowl compared with that of the fore cowl and to the boattail effect of the aft cowl.
4. The drag of the nacelle/diverter combination generally decreased with increasing Reynolds number.

NASA Langley Research Center
Hampton, VA 23681-0001
March 29, 1995

Appendix A

Measurements of Boundary-Layer Thickness

A boundary-layer survey was conducted on the flat-plate surface at a location where the plane of the nacelle inlet intersected the plate surface. This survey was used to determine the boundary-layer thickness approaching the nacelle so that the nacelle lip could be positioned relative to this thickness. A photograph and sketch of the rake used in this survey are shown in figure A1. The rake pressures were measured with a 5-psi electronically scanned pressure transducer.

Measurements of the initial boundary-layer profile showed that the measured stagnation pressure just outside the boundary layer was slightly higher than $p_{0,2}$ (the stagnation pressure immediately behind the shock wave). An example of these data is shown in figure A2. This trend was believed to be caused primarily by an oblique shock wave that emanated from the gap between the filler plate and pallet. The mechanism for causing this shock wave is unknown; however, it is hypothesized that it could be caused either by the flow expanding into the gap and impinging on the pallet lip face or by air entering the flow at the gap and causing a thickening of the boundary layer which created an oblique shock.

The gap between the filler plate and pallet was originally 0.015 in. wide. Tests were conducted both with the gap completely filled with dental plaster and with a foam seal mounted between the bottom surface of the filler plate and the pallet to prevent air from passing to and from the flat plate and instrumentation cavity, as shown in figure A3. The results from these tests showed no essential difference between the boundary-layer profiles with and without the foam seal, although using the dental plaster to fill the gap eliminated the stagnation pressures higher than free stream that were measured just outside the boundary layer. Therefore, these data indicate that the width of the gap was the primary factor in the boundary-layer-profile problem rather than the air passing to and from the flat-plate surface and the instrumentation cavity.

In order to minimize the effect of the gap on the boundary layer, strips of adhesive tape were placed on

the sides of the pallet to reduce the filler plate and pallet gap to approximately 0.005 in. The gap-width reduction improved the boundary-layer profile but did not completely eliminate the stagnation pressure higher than free stream just outside the boundary layer, as shown in figure A4.

After modifying the filler plate and pallet gap, the boundary-layer thickness approaching the nacelle was derived from boundary-layer surveys obtained at Mach numbers of 1.50, 1.80, 2.10, and 2.40 and Reynolds numbers ranging from 2.00×10^6 to 5.00×10^6 per foot. To determine the boundary-layer thickness (δ), the measured boundary-layer pressure coefficients were plotted against the probe height, as shown in figure A5. The intersection of a straight line drawn through the points outside the boundary layer and a straight line drawn through the last few points just inside the boundary layer was taken to be the boundary-layer thickness.

The measured boundary-layer profiles at each of the test conditions are shown in figure A6. The following table contains the boundary-layer thicknesses derived from the boundary-layer profiles:

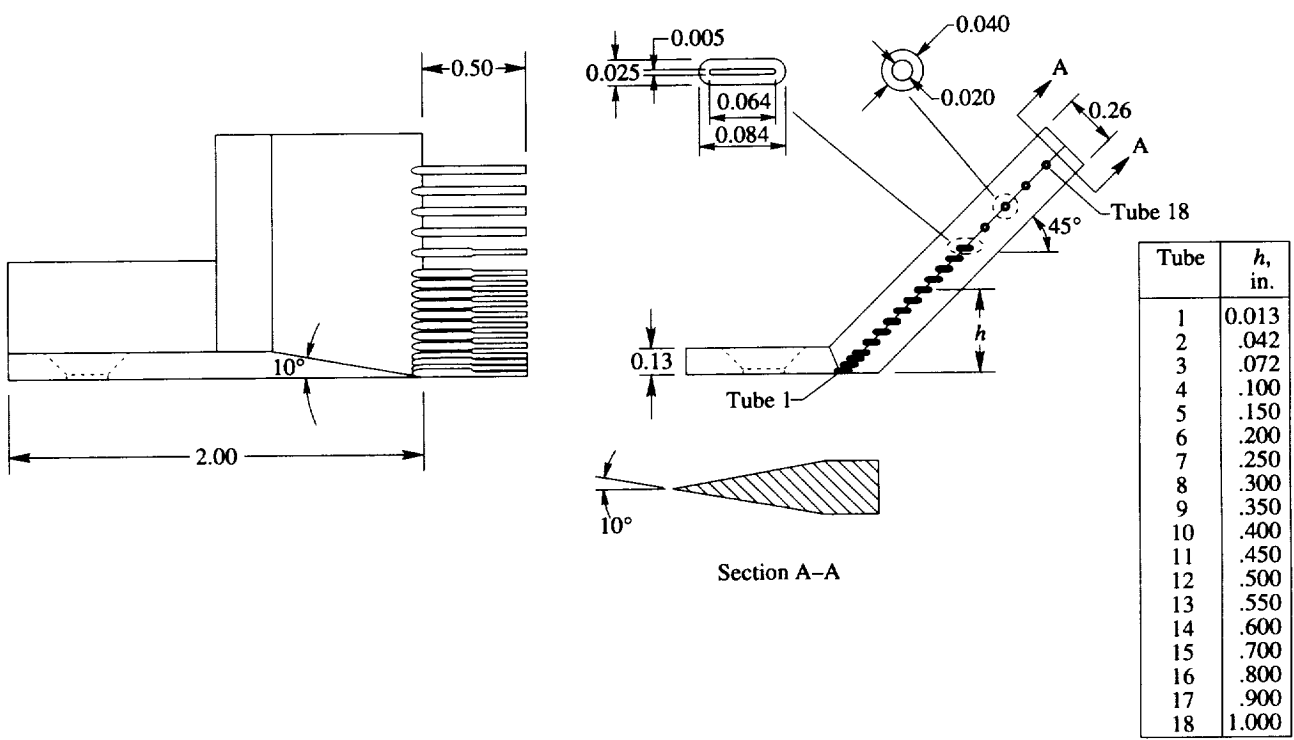
<i>R</i> , per foot	Values of boundary-layer thickness (δ), in., at—			
	<i>M</i> = 1.50	<i>M</i> = 1.80	<i>M</i> = 2.10	<i>M</i> = 2.40
2.00×10^6	0.21	0.20	0.22	0.23
3.00	.21	.20	.22	.22
4.00	.19	.18	.21	.22
5.00				.22

The boundary-layer thicknesses plotted against Reynolds number and Mach number are shown in figures A7 and A8, respectively. These results show that the data on boundary-layer thickness generally follow expected trends; that is, boundary-layer thicknesses decrease with increasing Reynolds number and decreasing Mach number. In figure A8, a slight decrease occurs in the boundary-layer thickness at $M = 1.80$; the reason for this variation is unknown, although it probably results from the uncertainty in the data caused by the limited number of pressure probes in the rake.



L-93-12969

(a) Photograph of boundary-layer rake.



(b) Sketch of boundary-layer rake. All linear dimensions are given in inches.

Figure A1. Boundary-layer rake.

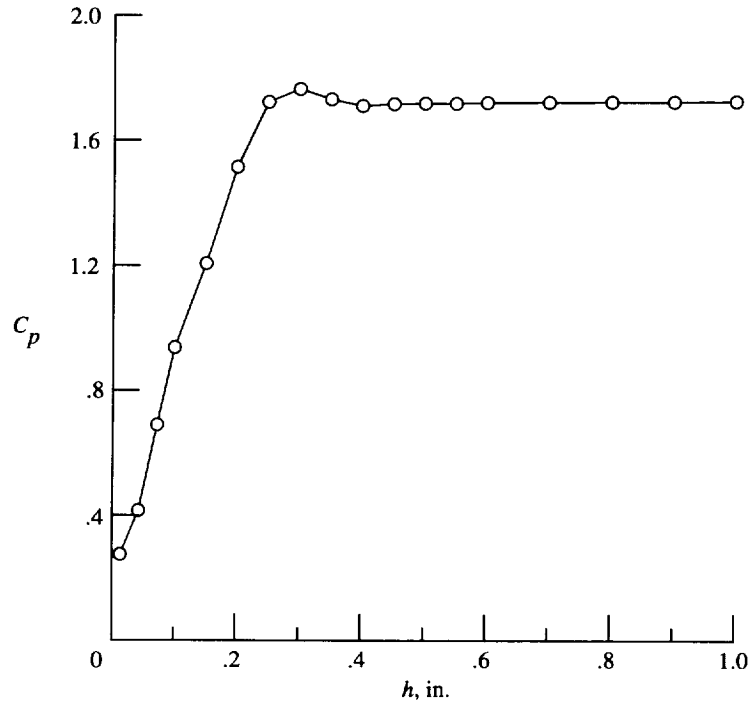


Figure A2. Initial boundary-layer profile at $M = 2.40$ and $R = 2.00 \times 10^6$ per foot.

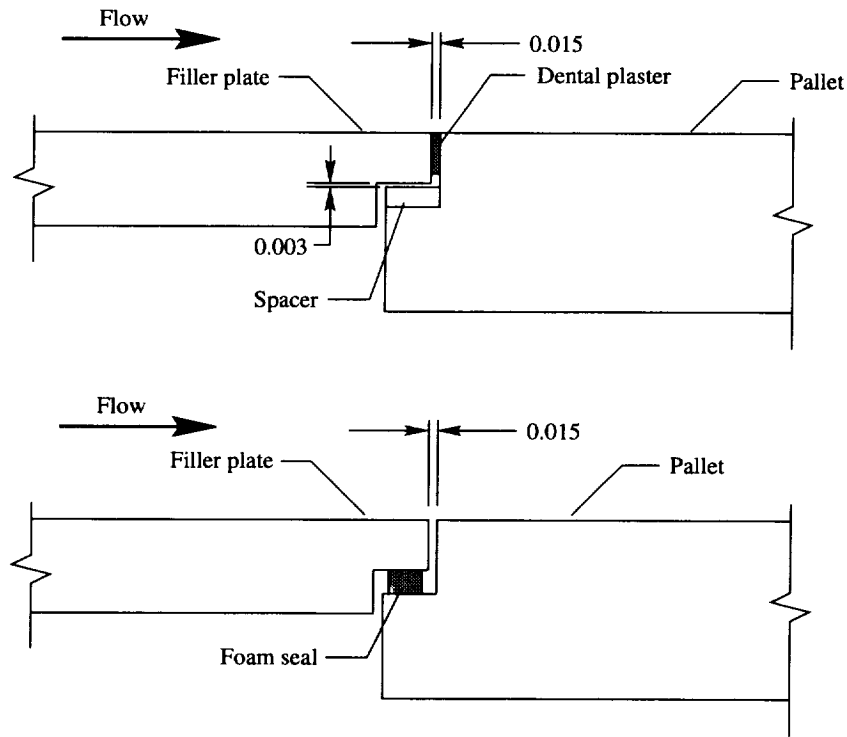


Figure A3. Configurations of temporary pallet and filler plate used to investigate boundary-layer profile problem. Sketches are not to scale; all dimensions are given in inches.

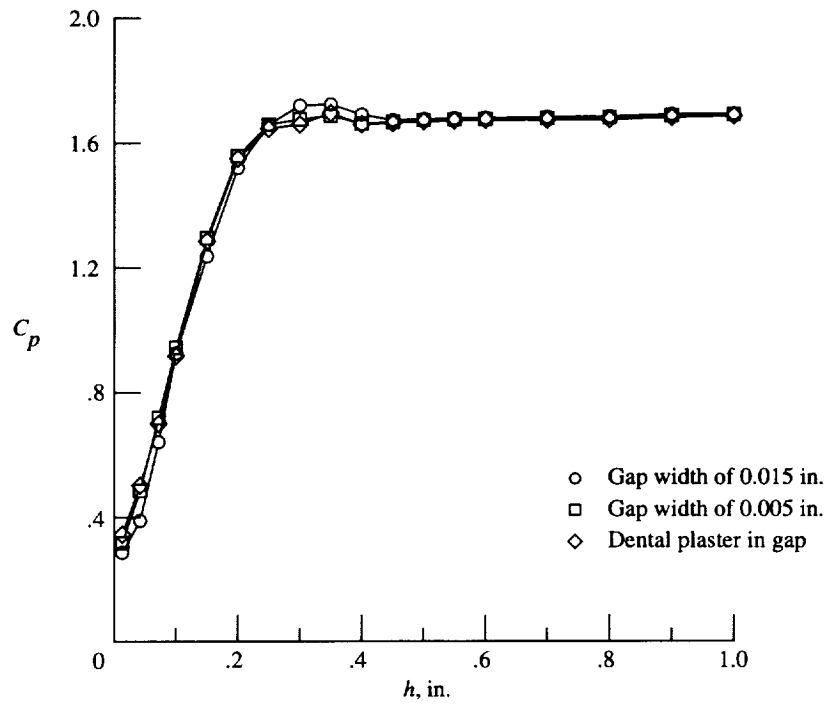


Figure A4. Comparison of boundary-layer profiles at $M = 2.10$ and $R = 2.00 \times 10^6$ per foot.

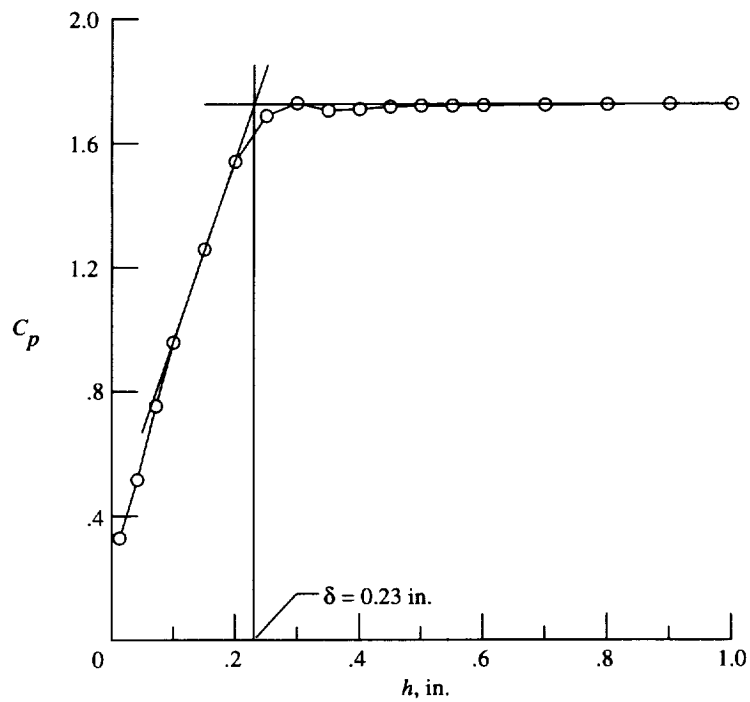
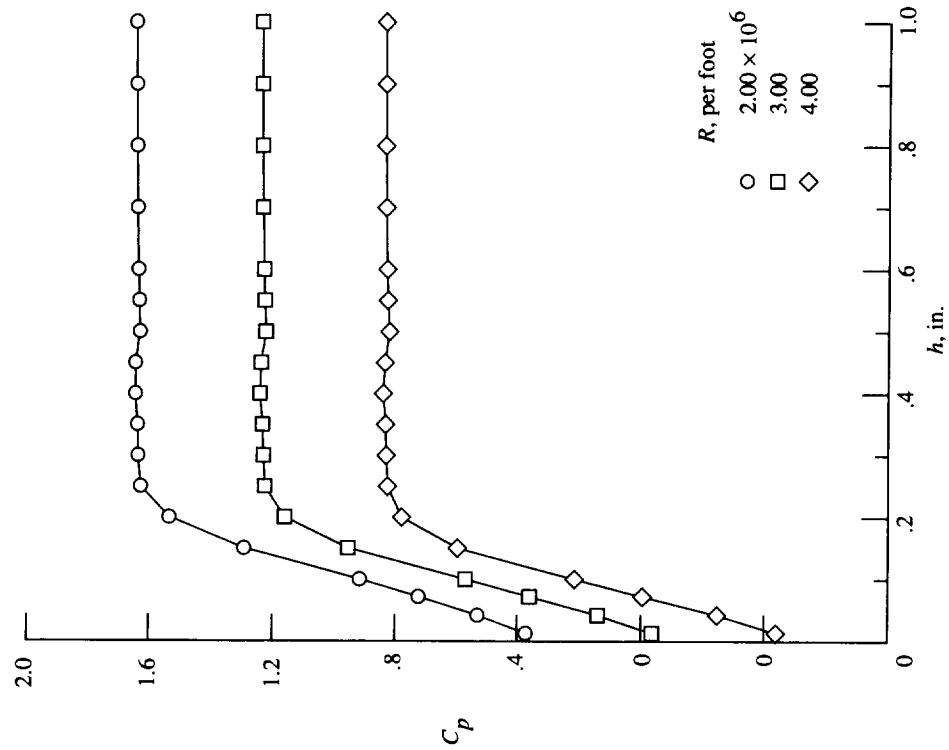
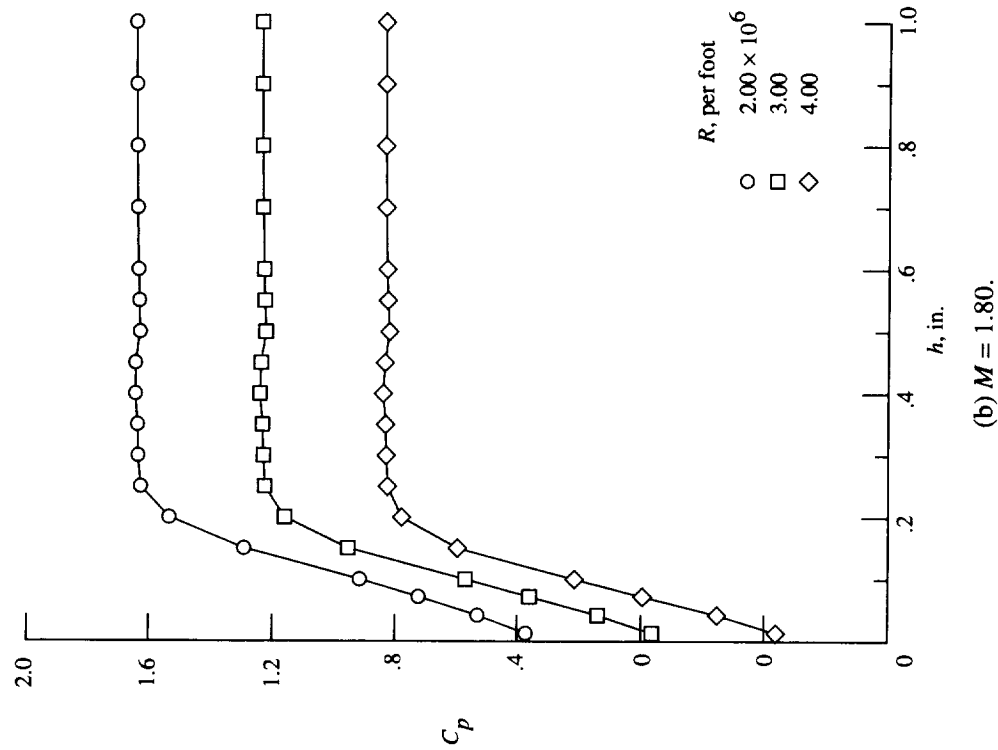


Figure A5. Determination of boundary-layer height at $M = 2.40$ and $R = 2.00 \times 10^6$ per foot.

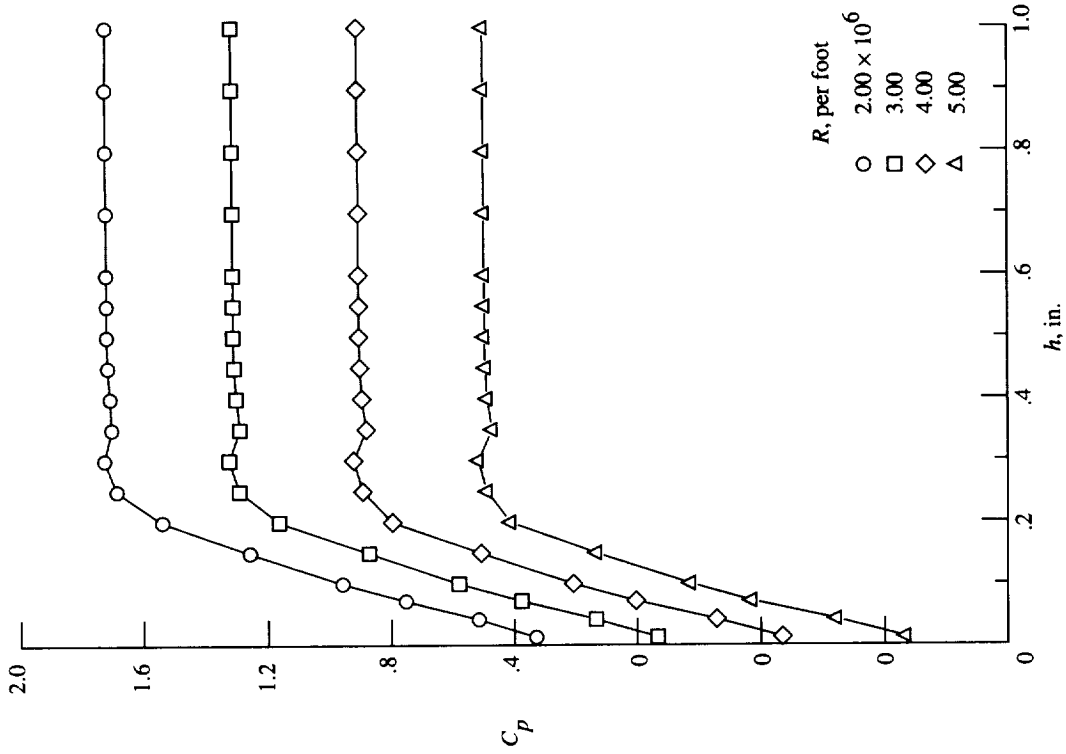


(a) $M = 1.50$.

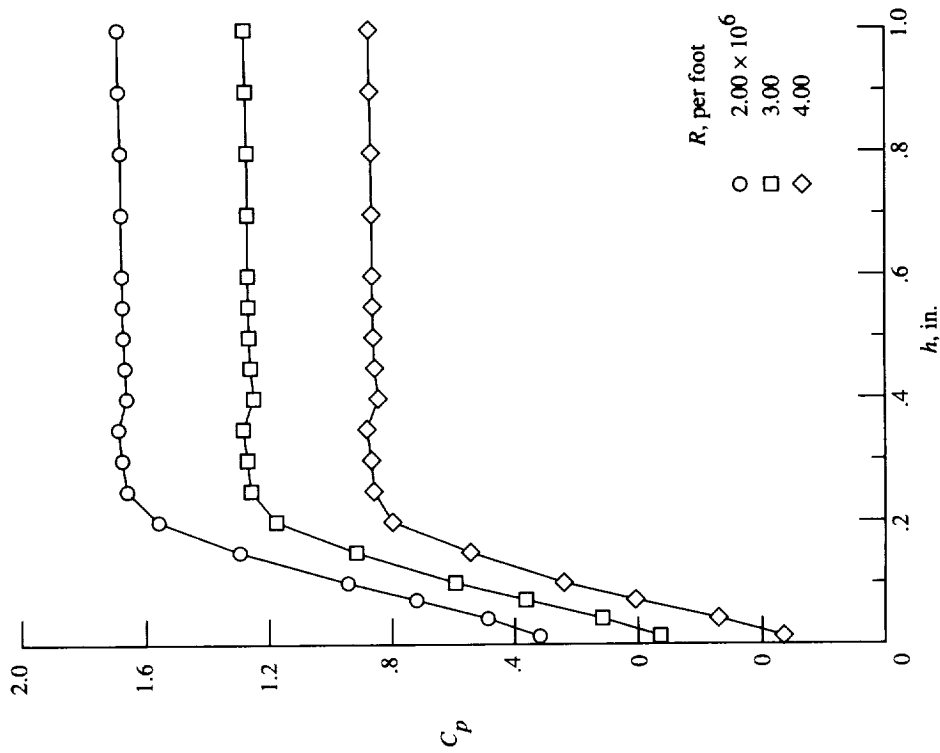


(b) $M = 1.80$.

Figure A6. Flat-plate boundary-layer profiles.



(d) $M = 2.40$.



(c) $M = 2.10$.

Figure A6. Concluded.

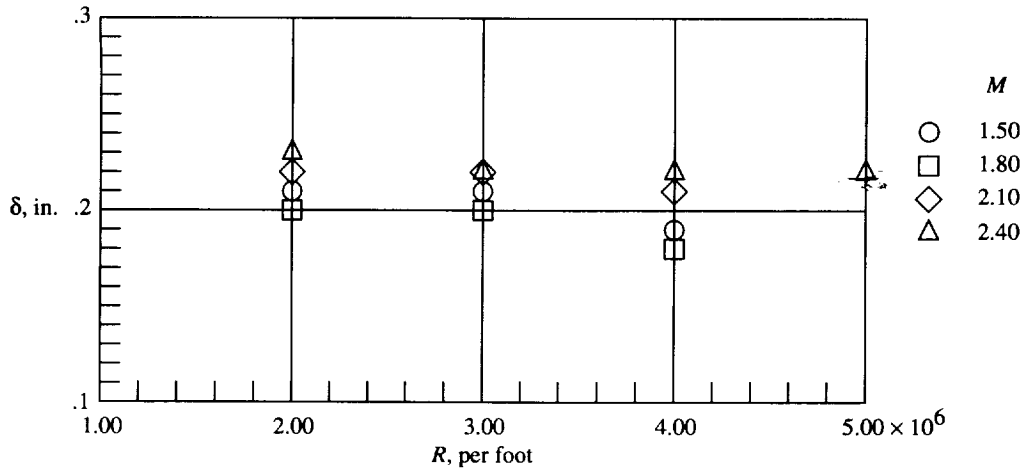


Figure A7. Effect of Reynolds number on measured flat-plate boundary-layer height.

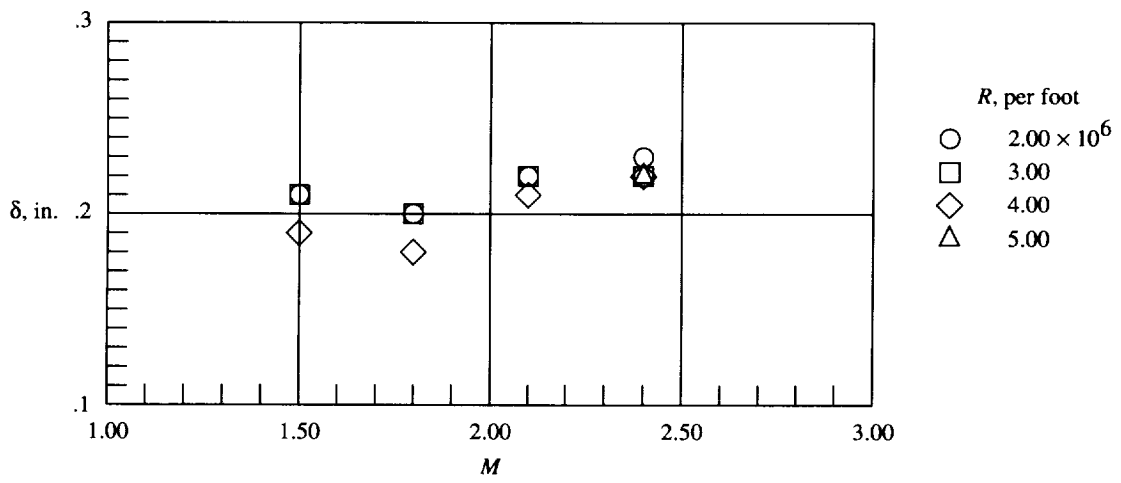


Figure A8. Effect of Mach number on measured flat-plate boundary-layer height.

Appendix B

Uncertainty Analysis of Experimental Data

The uncertainty of the drag measurements was calculated with the method discussed in reference 18. The experimental drag coefficient was calculated from seven variables as follows:

$$C_D = C_D(D, p_0, p_{al}, p_{fl}, M, W, \theta_f) \\ = \frac{D + W \sin \theta_f + (p_{al} - p_{fl}) A_l}{0.7 M^2 p_0 (1 + 0.2 M^2)^{-3.5} S} \quad (B1)$$

where

- A_l area of pallet lip, 0.0009201 ft²
- D drag force, lb
- M free-stream Mach number
- p_{al} static pressure on pallet aft lip, lb/ft²
- p_{fl} static pressure on pallet forward lip, lb/ft²
- p_0 free-stream stagnation pressure, lb/ft²
- S reference area, 2.602 ft²
- W weight of nacelle, diverter, and pallet assembly, lb
- θ_f flow angle, deg

The uncertainty in C_D due to the uncertainty in each of the seven variables used to calculate C_D is expressed as

$$\omega_{C_D} = \left[\left(\frac{\partial C_D}{\partial D} \omega_D \right)^2 + \left(\frac{\partial C_D}{\partial p_0} \omega_{p_0} \right)^2 + \left(\frac{\partial C_D}{\partial p_{al}} \omega_{p_{al}} \right)^2 \right. \\ \left. + \left(\frac{\partial C_D}{\partial p_{fl}} \omega_{p_{fl}} \right)^2 + \left(\frac{\partial C_D}{\partial M} \omega_M \right)^2 + \left(\frac{\partial C_D}{\partial W} \omega_W \right)^2 \right. \\ \left. + \left(\frac{\partial C_D}{\partial \theta_f} \omega_{\theta_f} \right)^2 \right]^{1/2} \quad (B2)$$

where

- ω_{C_D} uncertainty in C_D
- ω_D uncertainty in measured D , ± 0.0125 lb
- ω_{p_0} uncertainty in measured p_0 , ± 1.0 lb/ft²
- $\omega_{p_{al}}$ uncertainty in measured p_{al} , ± 1.0 lb/ft²
- $\omega_{p_{fl}}$ uncertainty in measured p_{fl} , ± 1.0 lb/ft²
- ω_M uncertainty in measured M , ± 0.02
- ω_W uncertainty in measured W , ± 0.0001 lb
- ω_{θ_f} uncertainty in measured θ_f , $\pm 0.005^\circ$

The uncertainty in C_D was calculated for each data point by using equation (B2). The largest uncertainty at each Mach number is given as follows:

M	Uncertainty in C_D
1.50	± 0.000013
1.80	± 0.000017
2.10	± 0.000020
2.40	± 0.000021

References

1. Nichols, Mark R.: *Aerodynamics of Airframe-Engine Integration of Supersonic Aircraft*. NASA TN D-3390, 1966.
2. Sigalla, Armand; and Hallstaff, Thomas H.: Aerodynamics of Powerplant Installation on Supersonic Aircraft. *J. Aircraft*, vol. 4, no. 4, July–Aug. 1967, pp. 273–277.
3. Welge, H. R.; Radkey, R. L.; and Henne, P. A.: Nacelle Integration Study on a Mach 2.2 Supersonic Cruise Aircraft. *J. Aircraft*, vol. 14, no. 11, Nov. 1977, pp. 1085–1092.
4. Kulfan, Robert M.: Application of Favorable Aerodynamic Interference to Supersonic Airplane Design. SAE Paper 901988, Oct. 1990.
5. Bencze, Daniel P.: *Experimental Evaluation of Nacelle-Airframe Interference Forces and Pressures at Mach Numbers of 0.9 to 1.4*. NASA TM X-3321, 1977.
6. Kulfan, Robert M.: Prediction of Nacelle Aerodynamic Interference Effects at Low Supersonic Mach Numbers. *Supersonic Cruise Research '79—Part 1*, NASA CP-2108, 1980, pp. 171–203.
7. Kulfan, R. M.; and Sigalla, A.: Airframe-Propulsion System Aerodynamic Interference Predictions at High Transonic Mach Numbers Including Off-Design Engine Airflow Effects. *Aerodynamics of Power Plant Installation*, AGARD-CP-301, Sept. 1981, pp. 35-1–35-23.
8. Middleton, W. D.; and Lundry, J. L.: *A System for Aerodynamic Design and Analysis of Supersonic Aircraft. Part I—General Description and Theoretical Development*. NASA CR-3351, 1980.
9. Morris, Odell A.; and Lamb, Milton: *Aerodynamic Characteristics at Mach Numbers of 2.30, 2.60, and 2.96 of a Domestic Supersonic Transport Configuration With a Fuselage Modified for Sonic-Boom Benefits*. NASA TM X-1830, 1969.
10. Radkey, R. L.; Welge, H. R.; and Felix, J. E.: *Aerodynamic Characteristics of a Mach 2.2 Advanced Supersonic Cruise Aircraft Configuration at Mach Numbers From 0.5 to 2.4*. NASA CR-145094, 1977.
11. Morris, Odell A.; Fuller, Dennis E.; and Watson, Carolyn B.: *Aerodynamic Characteristics of a Fixed Arrow-Wing Supersonic Cruise Aircraft at Mach Numbers of 2.30, 2.70, and 2.95*. NASA TM-78706, 1978.
12. Wilcox, Floyd J., Jr.: *Drag Measurements of Blunt Stores Tangentially Mounted on a Flat Plate at Supersonic Speeds*. NASA TP-2742, 1987.
13. Jackson, Charlie M., Jr.; Corlett, William A.; and Monta, William J.: *Description and Calibration of the Langley Unitary Plan Wind Tunnel*. NASA TP-1905, 1981.
14. Wassum, Donald L.; and Hyman, Curtis E., Jr.: *Procedures and Requirements for Testing in the Langley Research Center Unitary Plan Wind Tunnel*. NASA TM-100529, 1988.
15. Braslow, Albert L.; Hicks, Raymond M.; and Harris, Roy V., Jr.: *Use of Grit-Type Boundary-Layer-Transition Trips on Wind-Tunnel Models*. NASA TN D-3579, 1966.
16. Stallings, Robert L., Jr.; and Lamb, Milton: *Effects of Roughness Size on the Position of Boundary-Layer Transition and on the Aerodynamic Characteristics of a 55° Swept Delta Wing at Supersonic Speeds*. NASA TP-1027, 1977.
17. Wilcox, Floyd J., Jr.: *Experimental Investigation of Porous-Floor Effects on Cavity Flow Fields at Supersonic Speeds*. NASA TP-3032, 1990.
18. Holman, J. P.: *Experimental Methods for Engineers*, Third ed. McGraw-Hill Book Co., 1978.

Table I. Test Conditions

M	R , per foot	p_0 , lb/ft ²	T_0 , °F	q_∞ , lb/ft ²
1.50	2.00×10^6	1051	125	450.9
	3.00	1576	↓	676.3
	4.00	2102	↓	901.8
1.80	2.00×10^6	1154	125	455.5
	3.00	1731	↓	683.3
	4.00	2308	↓	911.0
2.10	2.00×10^6	1312	125	442.8
	3.00	1968	↓	664.2
	4.00	2623	↓	885.6
2.40	2.00×10^6	1520	125	419.1
	3.00	2280	↓	628.7
	4.00	3039	↓	838.2
	5.00	3799	↓	1047.8

Table II. Drag Data

(a) Nacelle/diverter configuration without aft cowl

M	R , per foot	θ , deg	h_n	h_n/δ	C_D
1.50	2.00×10^6	4.0	0.20	0.95	0.001246
	2.00	4.0	.24	1.14	.001277
	2.00	4.0	.35	1.67	.001367
	2.00	4.0	.49	2.33	.001475
	2.00	6.0	.20	.95	.001249
	1.99	6.0	.24	1.14	.001274
	2.00	6.0	.35	1.67	.001367
	2.00	6.0	.49	2.33	.001490
	2.00	8.0	.20	.95	.001247
	2.00	8.0	.24	1.14	.001289
	2.02	8.0	.35	1.67	.001385
	2.00	8.0	.49	2.33	.001523
	1.80	1.99×10^6	4.0	0.20	1.00
2.00		4.0	.24	1.20	.001104
2.00		4.0	.35	1.75	.001187
2.00		4.0	.49	2.45	.001278
1.99		6.0	.20	1.00	.001078
1.99		6.0	.24	1.20	.001106
2.00		6.0	.35	1.75	.001194
2.00		6.0	.49	2.45	.001292
1.99		8.0	.20	1.00	.001074
1.99		8.0	.24	1.20	.001111
2.01		8.0	.35	1.75	.001213
2.00		8.0	.49	2.45	.001324
2.10		1.99×10^6	4.0	0.20	0.91
	1.99	4.0	.24	1.09	.000960
	2.00	4.0	.35	1.59	.001015
	2.01	4.0	.49	2.23	.001091
	2.00	6.0	.20	.91	.000933
	1.99	6.0	.24	1.09	.000959
	1.99	6.0	.35	1.59	.001020
	2.00	6.0	.49	2.23	.001107
	1.99	8.0	.20	.91	.000931
	2.00	8.0	.24	1.09	.000963
	2.00	8.0	.35	1.59	.001041
	2.00	8.0	.49	2.23	.001144
	2.40	1.99×10^6	4.0	0.20	0.87
1.99		4.0	.24	1.04	.000838
1.99		4.0	.35	1.52	.000894
1.99		4.0	.49	2.13	.000958
2.00		6.0	.20	.87	.000818
1.99		6.0	.24	1.04	.000843
2.00		6.0	.35	1.52	.000905
2.00		6.0	.49	2.13	.000975
2.00		8.0	.20	.87	.000819
2.00		8.0	.24	1.04	.000856
2.00		8.0	.35	1.52	.000915
2.00		8.0	.49	2.13	.001001

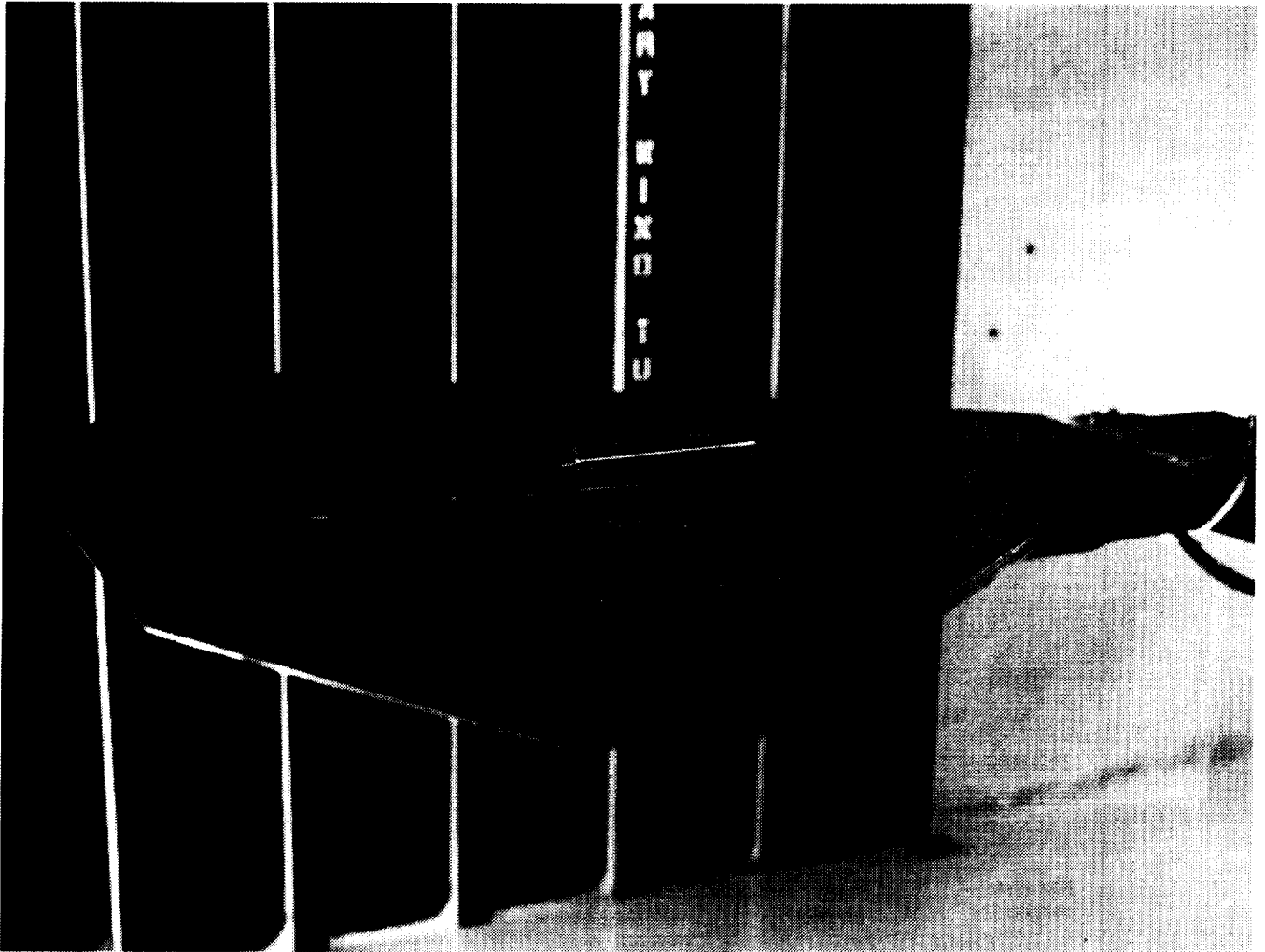
Table II. Concluded

(b) Nacelle/diverter configuration with aft cowl

M	R , per foot	θ , deg	h_n	h_n/δ	C_D
1.50	1.98×10^6	8.0	0.20	0.95	0.000954
	2.01	↓	.23	1.10	.000994
	1.99		.24	1.14	.001012
	2.01		.35	1.67	.001110
	2.01		.46	2.19	.001205
1.80	1.99×10^6	8.0	0.20	1.00	0.000897
	2.00	↓	.23	1.15	.000929
	2.00		.24	1.20	.000947
	2.00		.35	1.75	.001045
	1.99		.46	2.30	.001135
2.10	1.99×10^6	8.0	0.20	0.91	0.000819
	2.00	↓	.23	1.05	.000837
	1.99		.24	1.09	.000860
	1.99		.35	1.59	.000942
	1.99		.46	2.09	.001011
2.40	1.99×10^6	8.0	0.20	0.87	0.000750
	2.00	↓	.23	1.00	.000767
	2.00		.24	1.04	.000782
	2.00		.35	1.52	.000852
	1.98		.46	2.00	.000912

(c) Nacelle/diverter configuration without aft cowl with Reynolds number variation

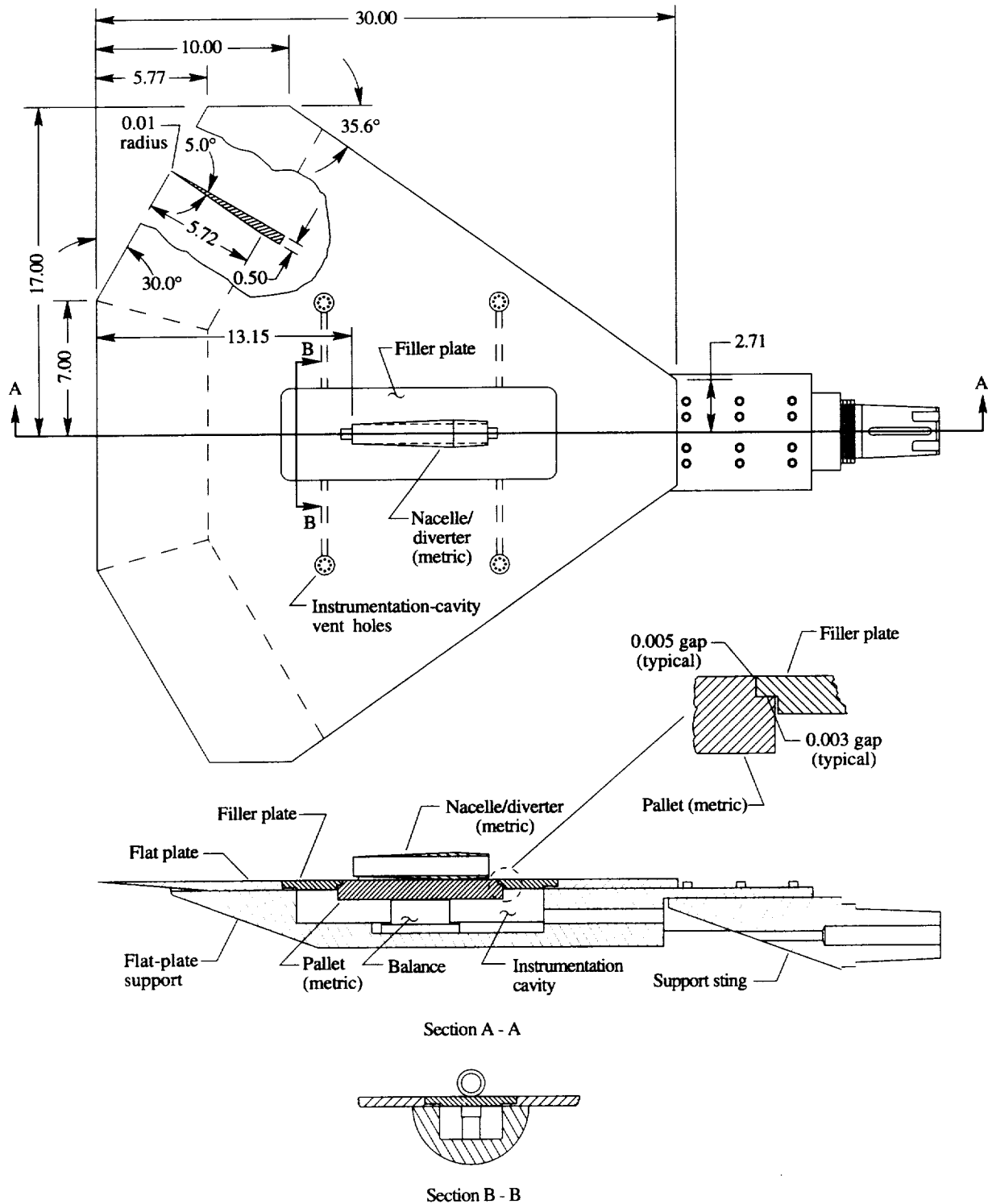
M	R , per foot	θ , deg	h_n	h_n/δ	C_D
1.50	2.00×10^6	8.0	0.24	1.14	0.001287
	3.00	8.0	.24	1.14	.001258
1.80	2.00×10^6	8.0	0.24	1.20	0.001116
	3.00	8.0	.24	1.20	.001086
	3.99	8.0	.24	1.33	.001070
2.10	1.99×10^6	8.0	0.24	1.09	0.000971
	2.99	8.0	.24	1.09	.000949
	3.98	8.0	.24	1.14	.000932
2.40	2.01×10^6	8.0	0.24	1.04	0.000851
	3.01	8.0	.24	1.09	.000839
	4.02	8.0	.24	1.09	.000841
	5.01	8.0	.24	1.09	.000820



L-93-01075

(a) Model mounted in wind tunnel

Figure 1. Description of flat-plate model.



(b) Schematic diagram of flat plate. All linear dimensions are given in inches.

Figure 1. Concluded.

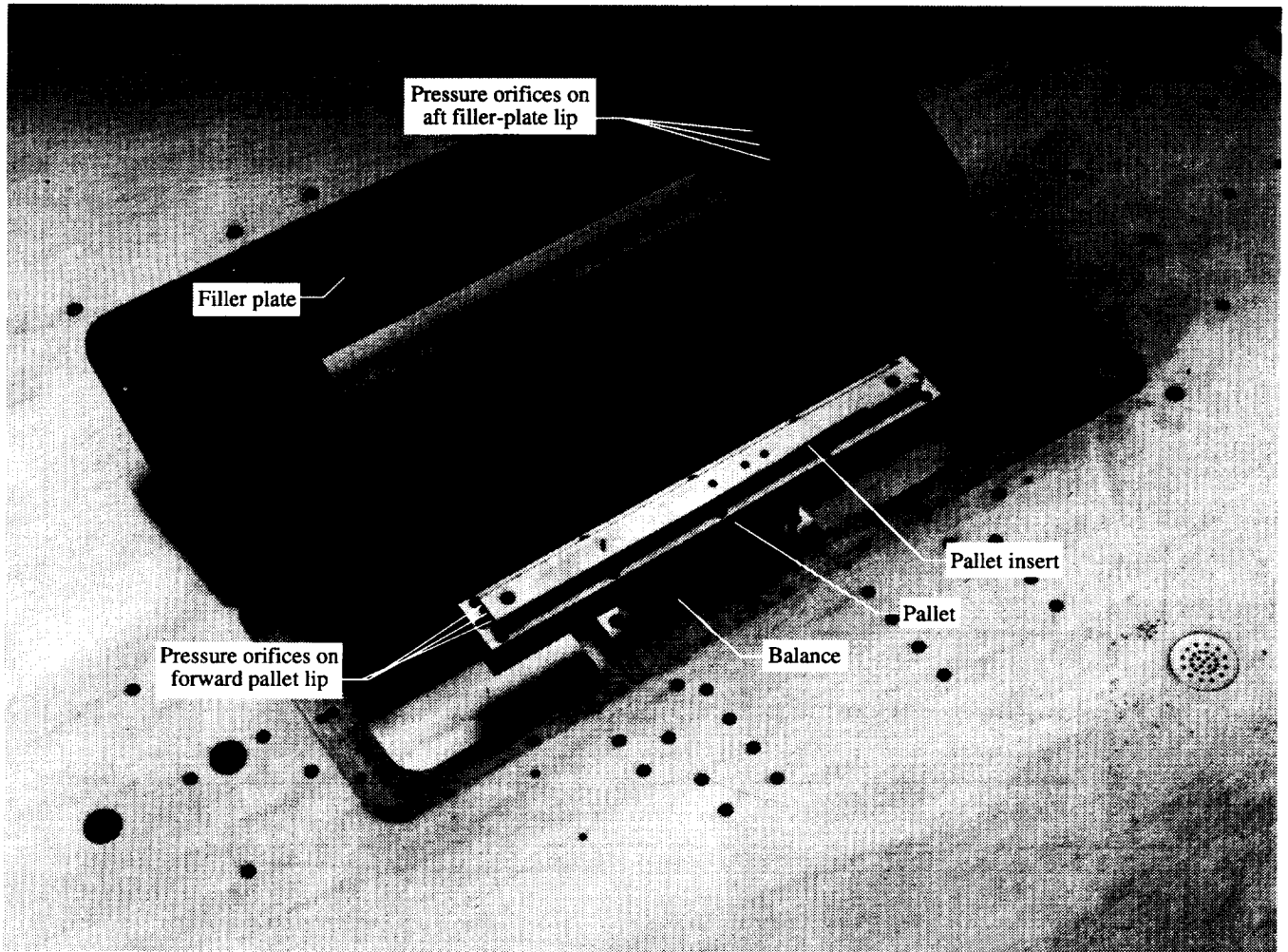
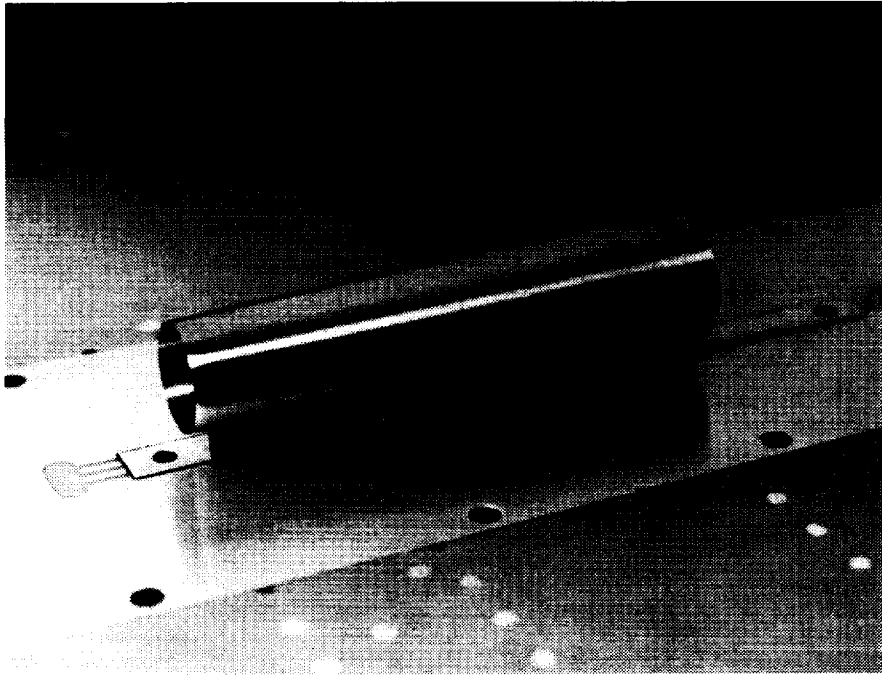


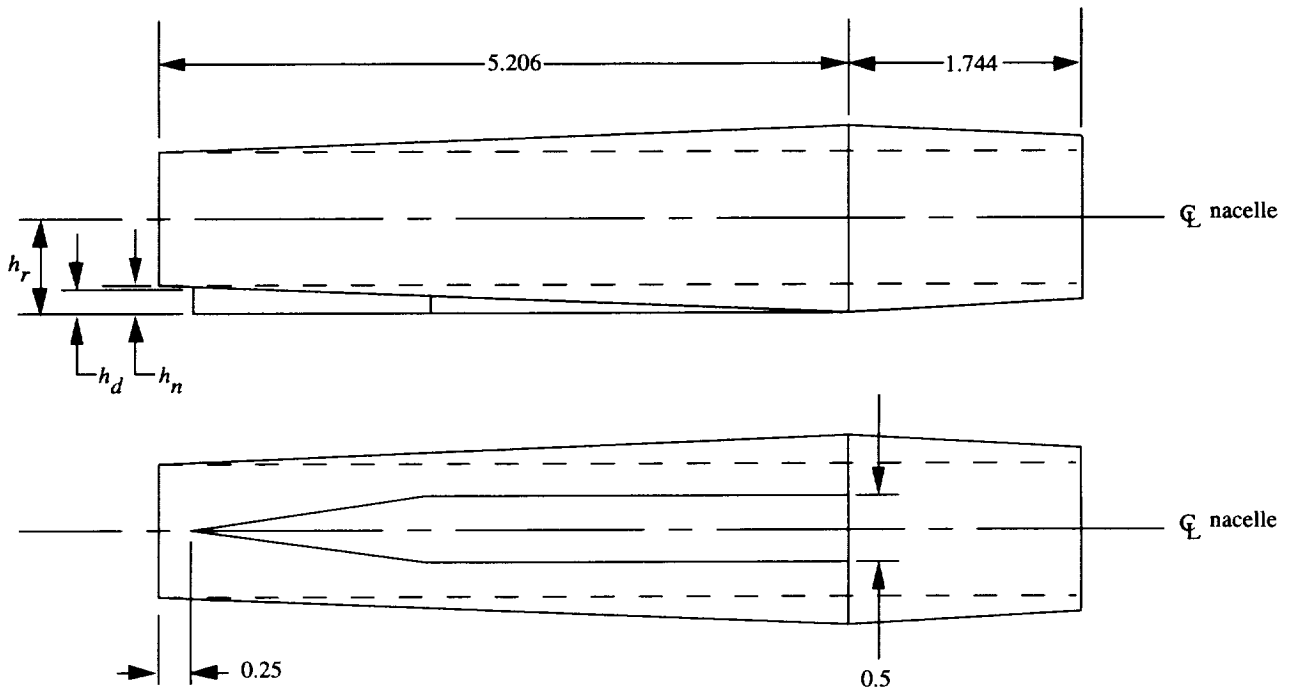
Figure 2. Instrumentation cavity of flat plate.

L-93-12972



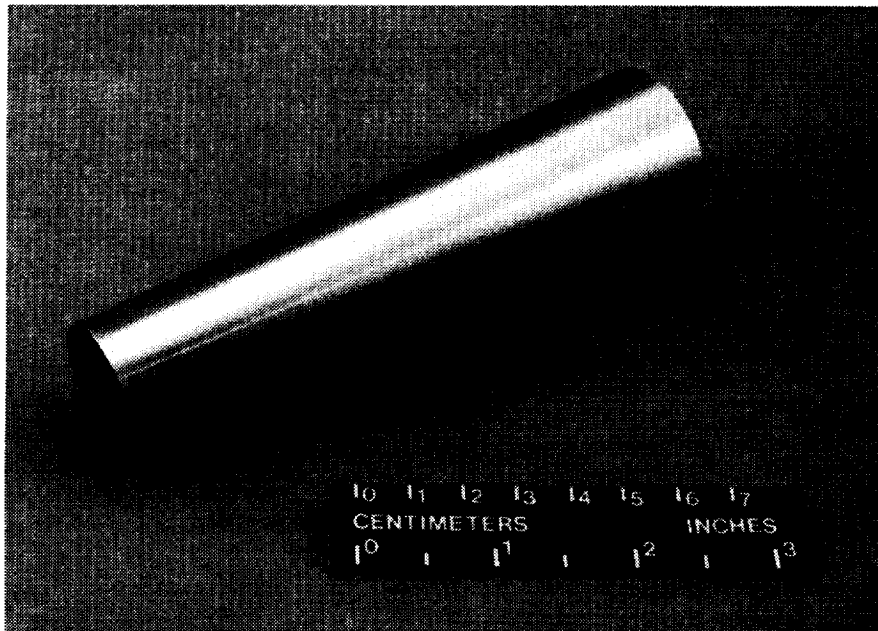
L-93-01074

(a) Photograph of assembly.



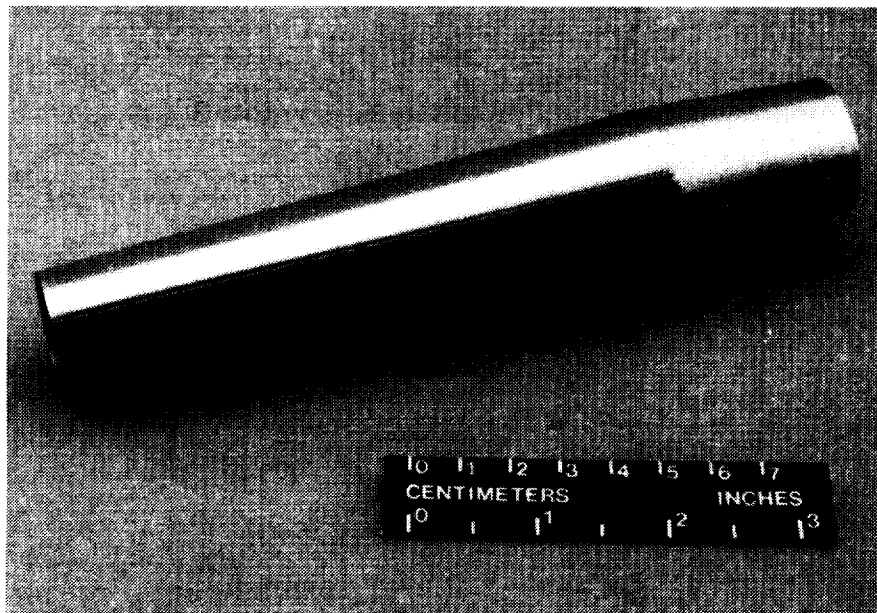
(b) Sketch of assembly with diverter 3 shown. All linear dimensions are given in inches.

Figure 3. Assembly of nacelle fore cowl and diverter on flat plate.



L-93-13147

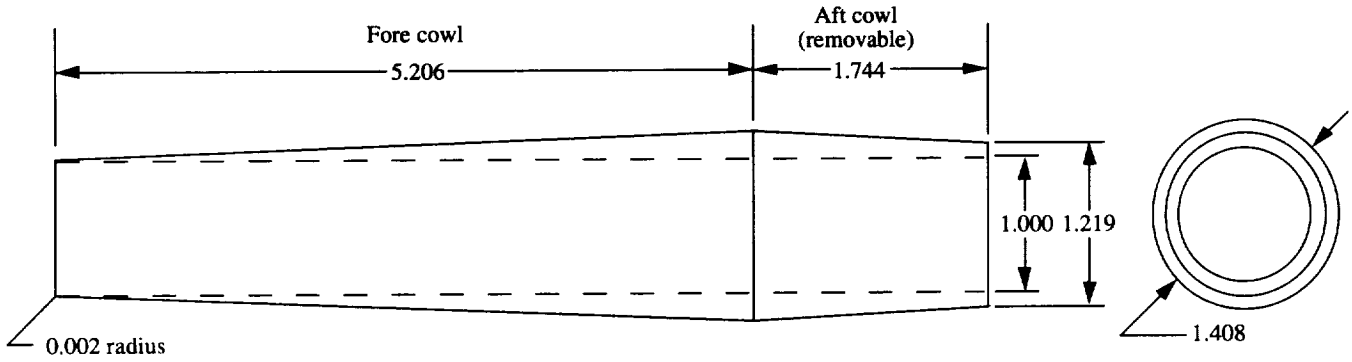
(a) Nacelle fore cowl.



L-93-13148

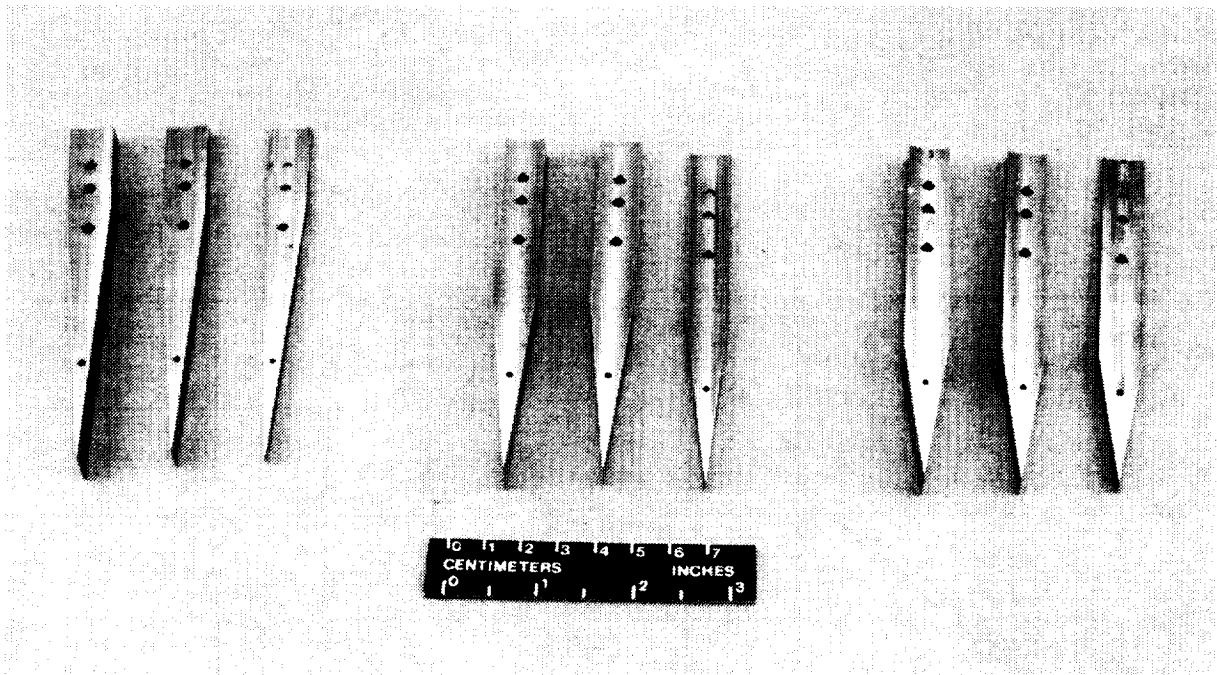
(b) Nacelle fore and aft cowls.

Figure 4. Photographs of nacelle.



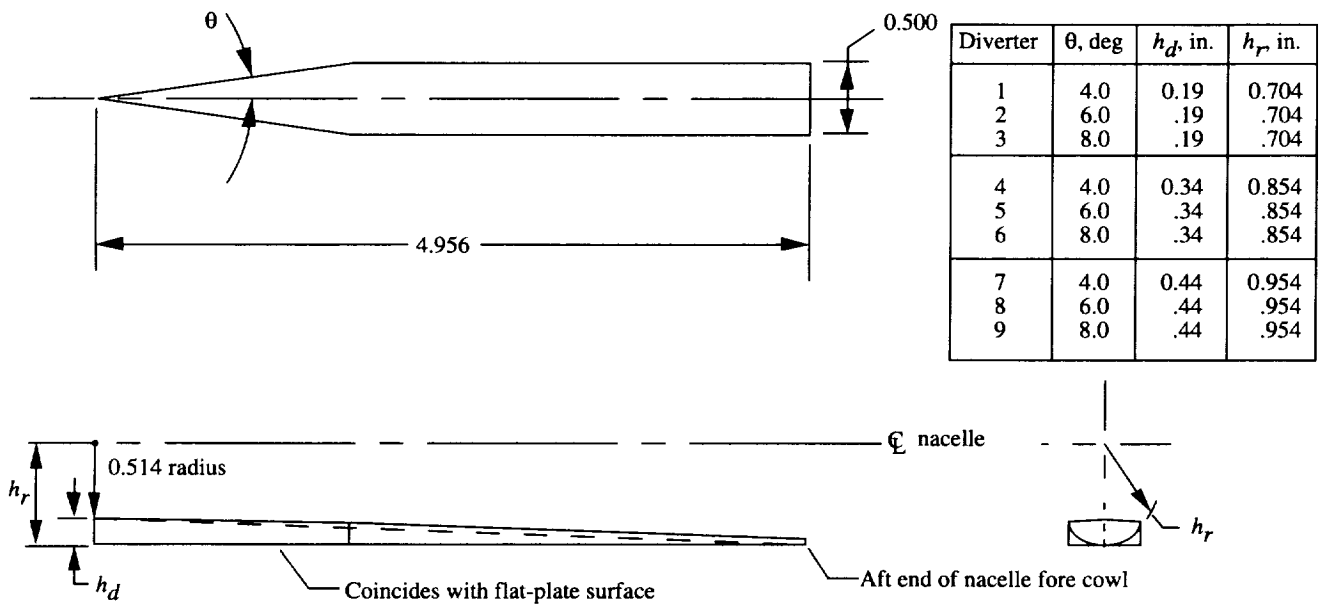
(c) Sketch of nacelle. All linear dimensions are given in inches.

Figure 4. Concluded.



L-93-13149

(a) Photograph of diverters.



(b) Sketch of diverter 3. All linear dimensions are given in inches.

Figure 5. Description of diverters.

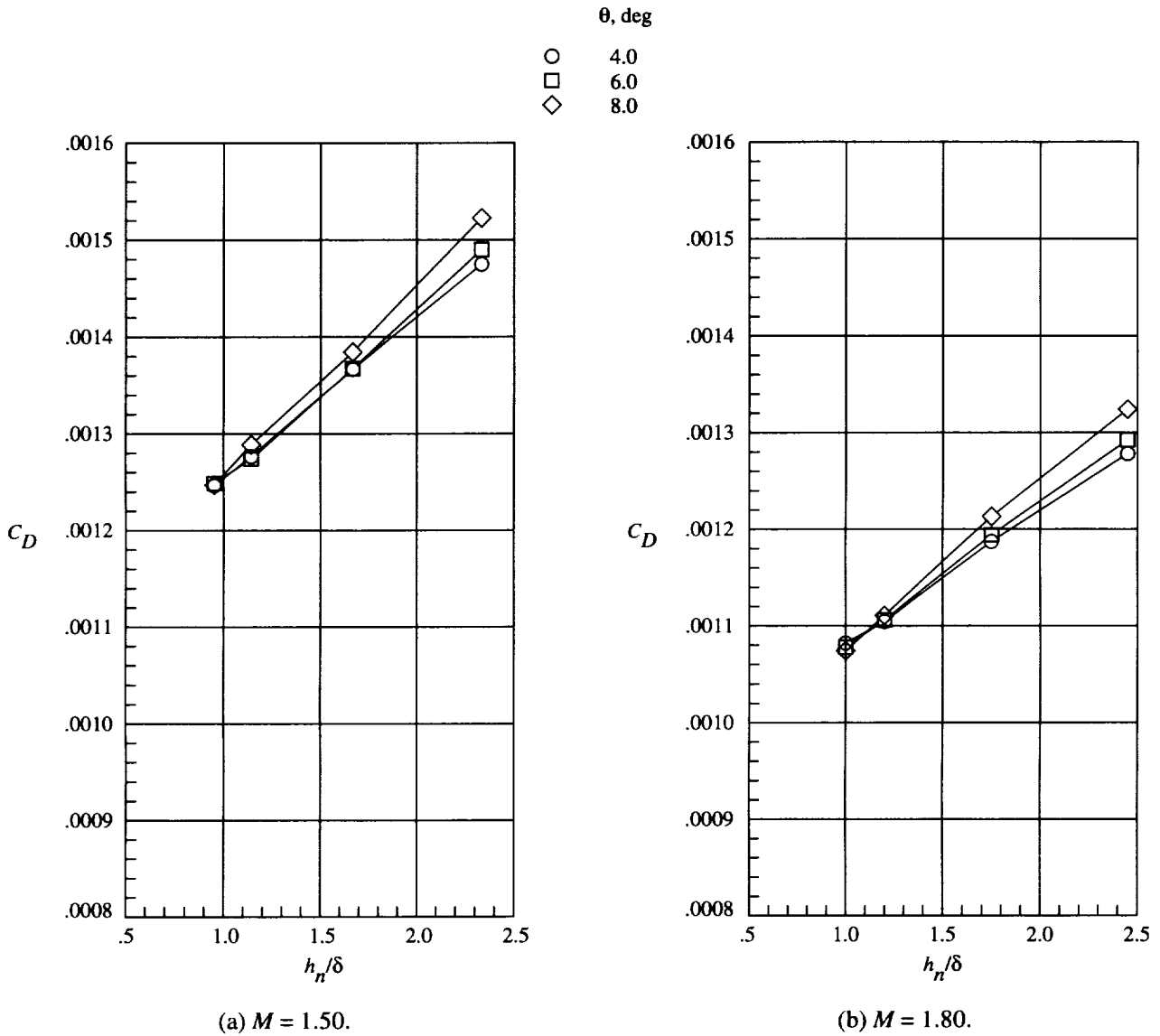


Figure 6. Effect of nacelle lip height on nacelle drag. Nacelle without aft cowl.

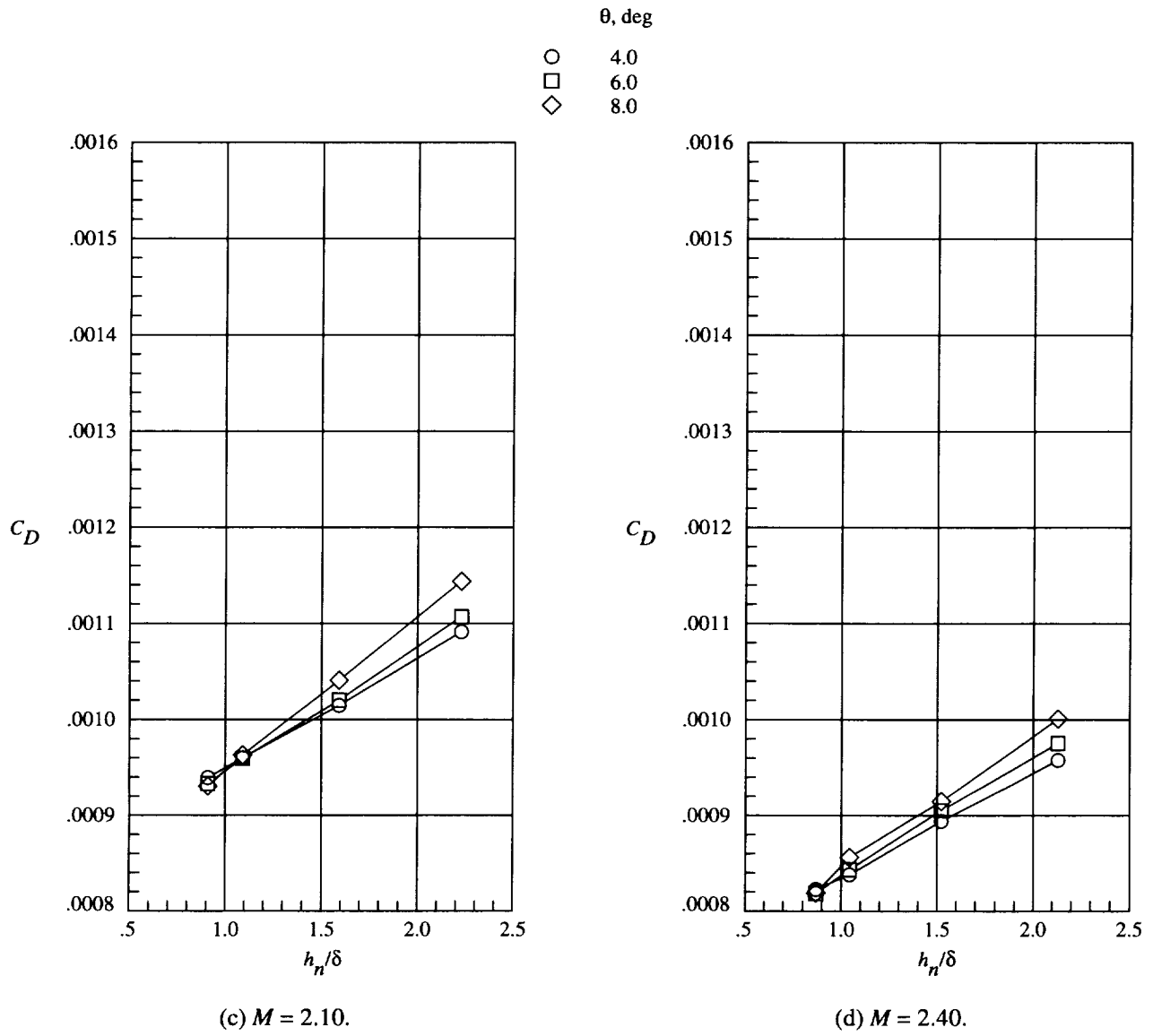
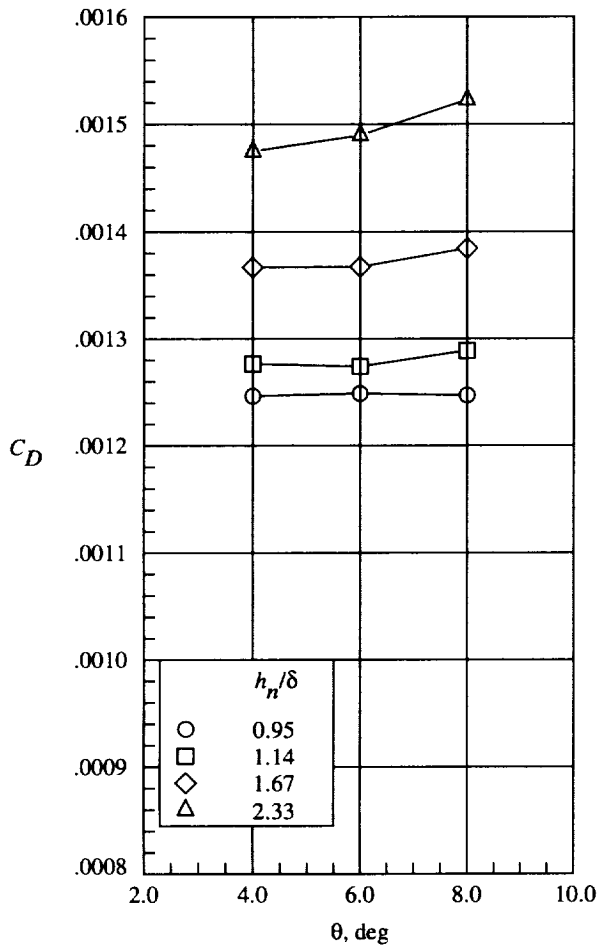
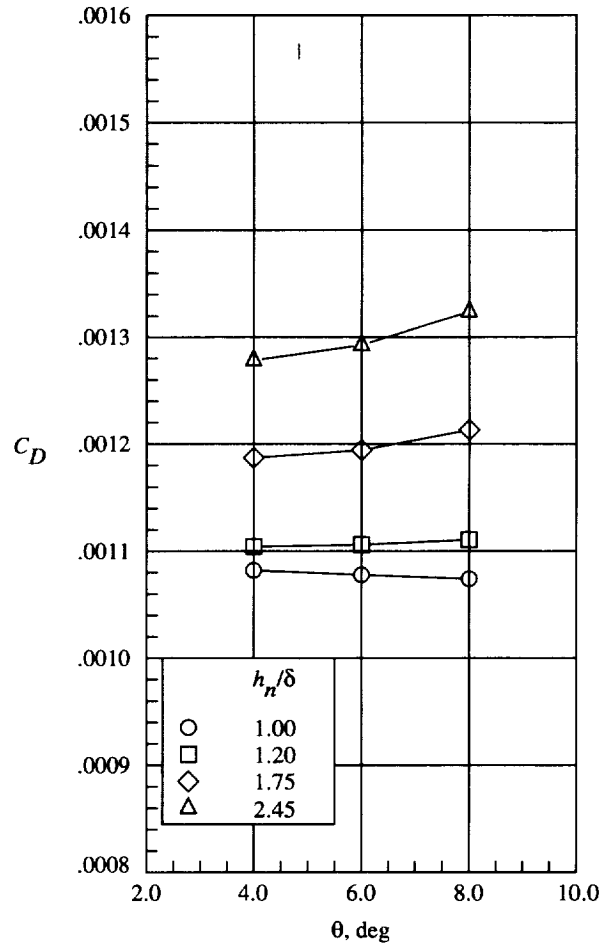


Figure 6. Concluded.

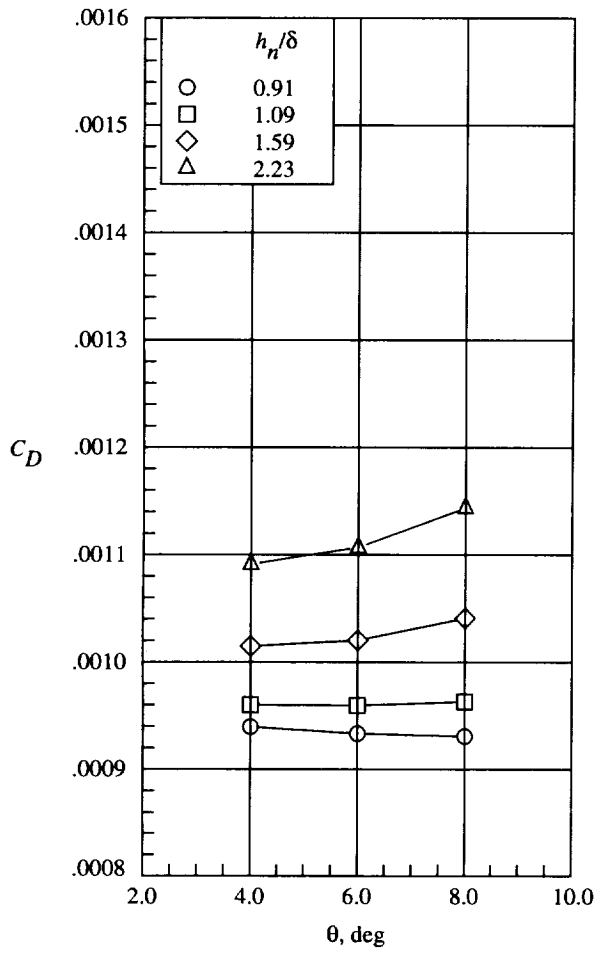


(a) $M = 1.50$.

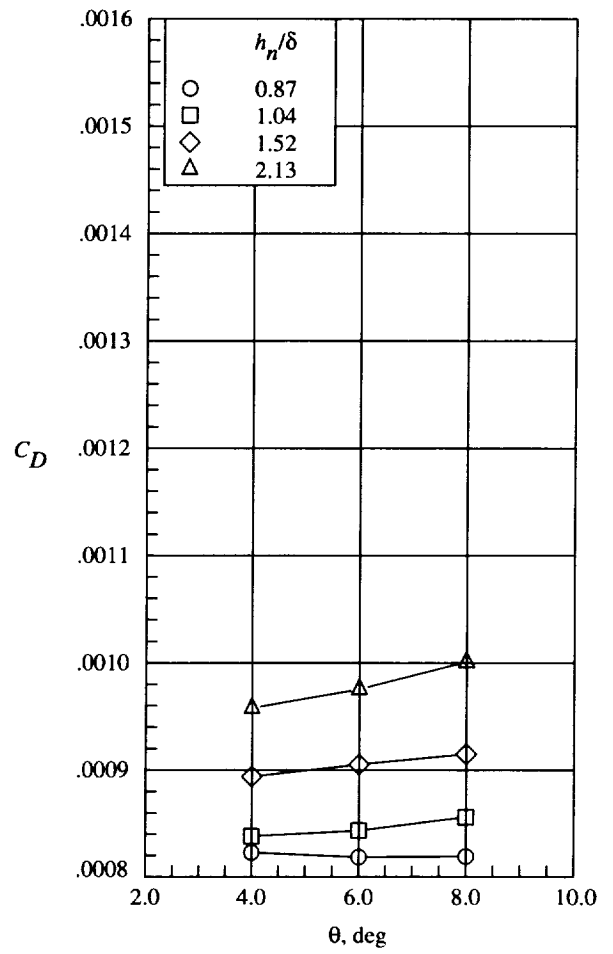


(b) $M = 1.80$.

Figure 7. Effect of diverter wedge half-angle on nacelle drag. Nacelle without aft cowl.

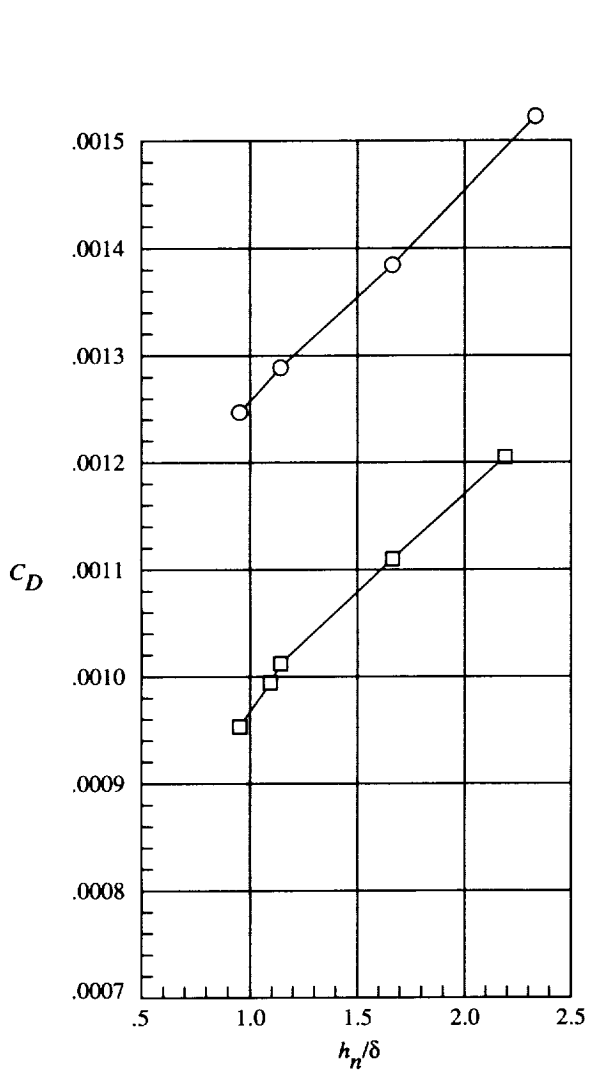


(c) $M = 2.10$.

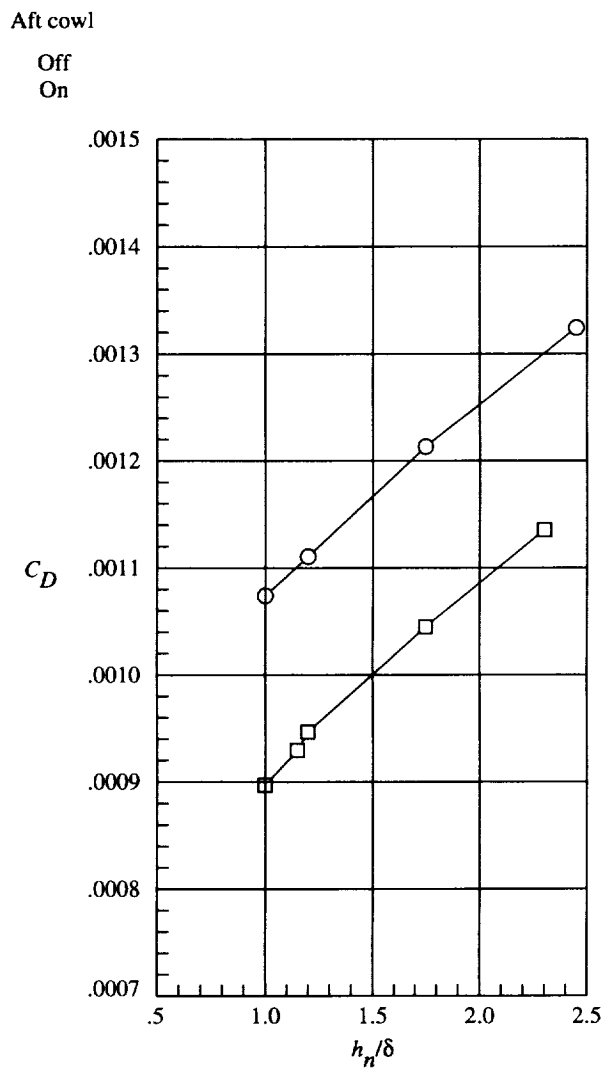


(d) $M = 2.40$.

Figure 7. Concluded.

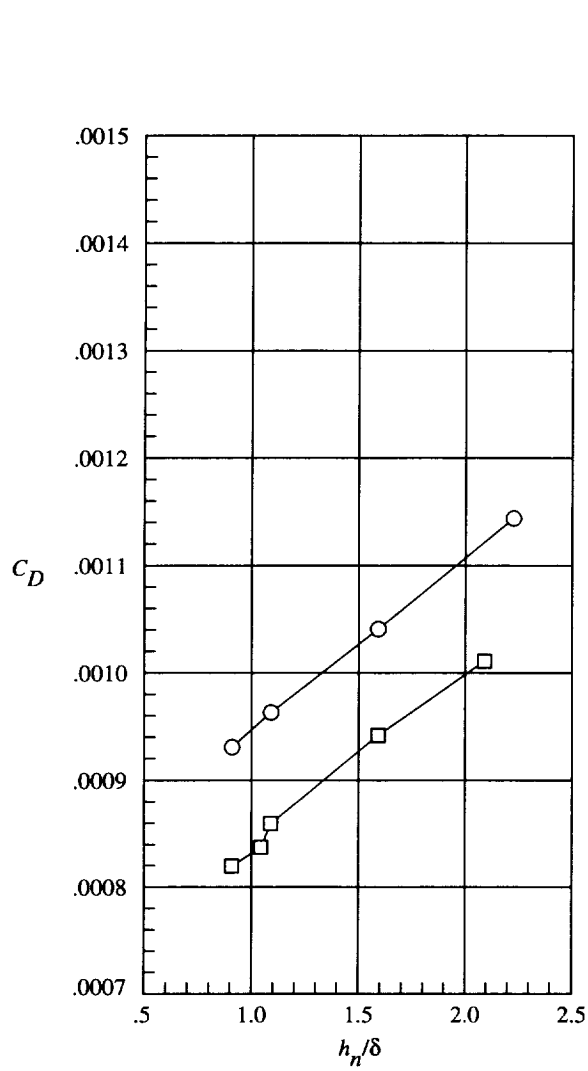


(a) $M = 1.50$.

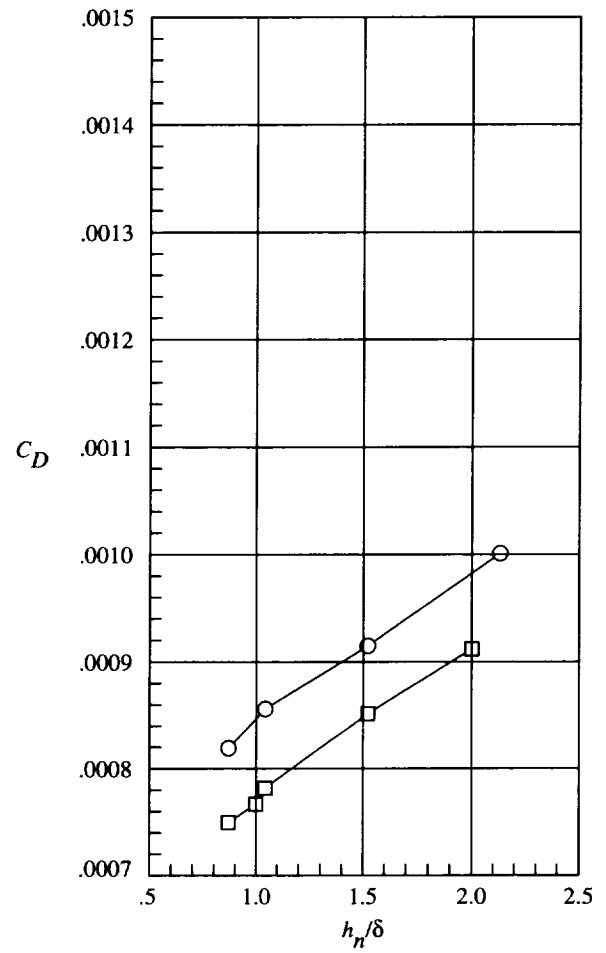


(b) $M = 1.80$.

Figure 8. Effect of aft cowl on nacelle drag at $\theta = 8.0^\circ$.



(c) $M = 2.10$.



(d) $M = 2.40$.

Figure 8. Concluded.

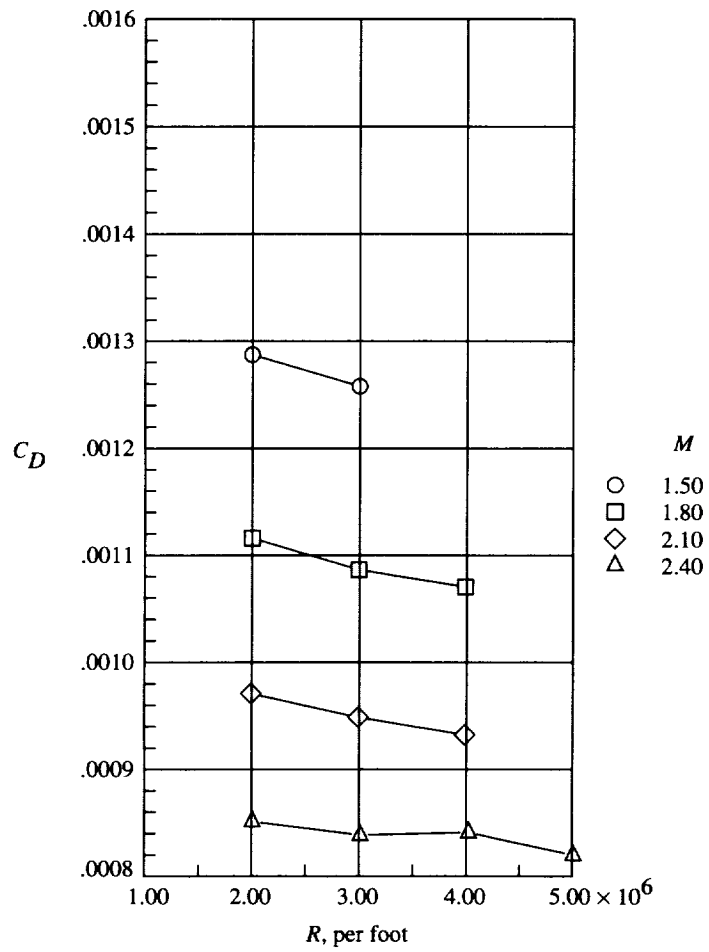


Figure 9. Effect of Reynolds number on nacelle/diverter drag. Nacelle without aft cowl; $\theta = 8.0^\circ$; $h_n = 0.24$ in.